Impact of ambient conditions on the Si isotope fractionation in marine pore fluids during early diagenesis

Sonja Geilert[1], Patricia Grasse[1], Kristin Doering[1,2], Klaus Wallmann[1], Claudia Ehlert[3], Florian Scholz[1], Martin Frank[1], Mark Schmidt[1], Christian Hensen[1]

[1]GEOMAR Helmholtz Centre for Ocean Research Kiel, Wischhofstr. 1-3, 24148 Kiel, Germany

[2]Department of Oceanography, Dalhousie University, Halifax, Canada

[3]Marine Isotope Geochemistry, ICBM, University of Oldenburg, Germany

ABSTRACT

Benthic fluxes of dissolved silicon (Si) from sediments into the water column are driven by the dissolution of biogenic silica ($bSiO_2$) and terrigenous Si minerals and modulated by the precipitation of authigenic Si phases. Each of these processes has a specific effect on the isotopic composition of silicon dissolved in sediment pore fluids such that the determination of pore fluid $\delta^{30}Si$ values can help to decipher the complex Si cycle in surface sediments. In this study, the $\delta^{30}Si$ signatures of pore fluids and $bSiO_2$ in the Guaymas Basin (Gulf of California) were analyzed, which is characterized by high $bSiO_2$ accumulation and hydrothermal activity. The $\delta^{30}Si$ signatures were investigated in the deep basin, in the vicinity of a hydrothermal vent field, and at an anoxic site located within the pronounced oxygen minimum zone (OMZ). The pore fluid $\delta^{30}Si_{pf}$ signatures differ significantly depending on the ambient conditions. Within the basin, $\delta^{30}Si_{pf}$ is essentially uniform averaging +1.2±0.1‰ (1SD). Pore fluid $\delta^{30}Si_{pf}$ values from within the OMZ are significantly lower (0.0±0.5‰, 1SD), while pore fluids close to the hydrothermal vent field are higher (+2.0±0.2‰, 1SD).

Reactive transport modelling results show that the $\delta^{30}Si_{pf}$ is mainly controlled by silica dissolution ($bSiO_2$ and terrigenous phases) and Si precipitation (authigenic aluminosilicates). Precipitation processes cause a shift to high pore fluid $\delta^{30}Si_{pf}$ signatures, most pronounced at the hydrothermal site. Within the OMZ however, additional dissolution of isotopically depleted Si minerals (e.g. clays) facilitated by high mass accumulation rates of terrigenous material (MAR_{terr}) is required to promote the low $\delta^{30}Si_{pf}$ signatures while precipitation of authigenic aluminosilicates seems to be hampered by high water/rock ratios. Guaymas OMZ $\delta^{30}Si_{pf}$ values are markedly different from those of the Peruvian OMZ, the only other marine OMZ setting where Si isotopes have been investigated to constrain early diagenetic processes. These differences highlight the fact that $\delta^{30}Si_{pf}$ signals in OMZs worldwide are not alike and each setting can result in a range of $\delta^{30}Si_{pf}$ values as a function of the

environmental conditions. We conclude that the benthic silicon cycle is more complex than previously thought and that additional Si isotope studies are needed to decipher the controls on Si turnover in marine sediment and the role of sediments in the marine silicon cycle.

KEYWORDS: Si isotopes, reverse weathering, hydrothermal system, oxygen minimum zone, environmental conditions

1. INTRODUCTION

Silicon (Si) is one of the key macronutrients in the ocean mainly utilized by siliceous organisms such as diatoms, radiolarians or sponges (see recent review by Sutton et al., 2018). The marine Si cycle is closely linked to the carbon (C) cycle by marine siliceous organisms, which transport C to the sediment and thus exert a strong control on C export from the atmosphere impacting present and past climate (e.g. Lewin, 1961; Tréguer and Pondaven, 2000; Tréguer and De La Rocha, 2013; and recent reviews by Frings et al., 2016 and Sutton et al., 2018). Studies of Si isotopes ($\delta^{30}Si$) have revealed complex uptake and dissolution processes of siliceous organisms, which have a dominant control on the $\delta^{30}Si$ distribution in ocean waters (e.g. De La Rocha et al., 1997; Varela et al., 2004; Cardinal et al., 2005; Beucher et al., 2008; Fripiat et al., 2011; Ehlert et al., 2012; Grasse et al., 2013; Sutton et al., 2013; de Souza et al., 2014, 2015). Diatoms constitute the largest part of the Si cycling fluxes in the ocean (Ragueneau et al., 2000) and discriminate between its isotopes during Si uptake, whereby the light isotopes are preferentially incorporated into the diatom frustules (e.g. De La Rocha et al., 1997). Si isotope fractionation during Si uptake is dependent on e.g. the diatom species, the availability of Fe, and the degree of Si utilization. Fractionation factors between -0.5 and -2.1‰ have been derived from regional water mass mixing and laboratory studies (De La Rocha et al., 1997; Varela et al., 2004; Cardinal et al., 2005; Beucher et al., 2008; Sutton et al., 2013; Meyerink et al., 2017).

After a planktonic bloom whereupon the nutrients are exhausted, biogenic silica ($bSiO_2$, mainly diatoms) sinks through the ocean, partially dissolves and accumulates on the seafloor, where its preservation and recycling is controlled by dissolution and Si re-precipitation processes. The dissolution of $bSiO_2$ mainly controls the accumulation of silicic acid ($Si(OH)_4$) in pore fluids, although the in-situ concentration remains below the equilibrium concentration of dissolved $bSiO_2$, which has been explained by simultaneous formation of authigenic silicates (e.g. McManus et al., 1995; Van Cappellen and Qiu, 1997a, b; Rickert et al., 2002). This process is termed reverse weathering given that the authigenic precipitates are rich in seawater-derived cations, like Na, K or Mg (Mackenzie et al., 1981; Michalopoulos and Aller, 1995). Experimental studies of $bSiO_2$ dissolution kinetics revealed

a dependence of the $bSiO_2$ reactivity on sediment depth as well as the ratio between terrigenous material and $bSiO_2$ (Michalopoulos and Aller, 1995; Van Cappellen and Qiu, 1997a, b; Dixit et al., 2001; Rickert et al., 2002). Marine weathering of terrigenous material (primary silicates like feldspars and secondary silicates like clays), was found to release cations such as aluminum (Al) or iron (Fe), which reduce the solubility and dissolution rate of $bSiO_2$ and induce aluminosilicate precipitation (Michalopoulos and Aller, 1995; Van Cappellen and Qiu, 1997a, b; Michalopoulos et al., 2000; Dixit et al., 2001; Rickert et al., 2002; Loucaides et al., 2010). The accumulation of Si in pore fluids and the Si reflux into bottom waters are controlled by three interdependent processes, namely: opal dissolution, dissolution of terrigenous solids, precipitation of authigenic minerals.

Early silica diagenesis has been shown to fractionate Si isotopes as a function of the crystallization state, seawater Si concentration, sedimentation rate, and terrigenous mineral content (Tatzel et al., 2015; Geilert et al., 2016). Since the light ^{28}Si isotope is more reactive compared to the heavier isotopes (^{29}Si, ^{30}Si) , processes such as reverse weathering, adsorption, and direct Si precipitation from saturated solutions show low $\delta^{30}Si$ values in the reaction product and high $\delta^{30}Si$ values in its substrate (i. e. fluids) (e.g. Georg et al., 2006a, 2009; Delstanche et al., 2009; Opfergelt et al., 2013; Geilert et al., 2014; Roerdink et al., 2015; Ehlert et al., 2016). The few modelling and experimental studies, addressing Si isotope fractionation during formation of secondary phases, report isotope fractionation factors between -1.6 and -2‰ (Ziegler et al., 2005; Méheut et al., 2007; Dupuis et al., 2015; Ehlert et al., 2016).

The $\delta^{30}Si$ data for marine pore fluids from the Peruvian margin upwelling region, which is characterized by very high diatom productivity and $bSiO_2$-rich sediments (Abrantes et al., 2007; Bruland et al., 2005), agree with these findings and clearly indicate Si isotope fractionation as a consequence of authigenic aluminosilicate precipitation accompanied by a Si isotope fractionation factor of -2.0‰ (Ehlert et al., 2016). Also pore fluids from the Greenland margin and Labrador Sea reflect early diagenetic reactions detected by pore fluid $\delta^{30}Si$ values (between +0.76 and +2.08‰) and the $\delta^{30}Si$ values were interpreted as the product of reverse weathering reactions (Ng et al., 2020). In this study, the Guaymas Basin in the Gulf of California was chosen as study area, as it is characterized by a relatively high diatom productivity and sediments that are predominantly composed of diatomaceous muds (up to 50% diatoms; Kastner and Siever, 1983). Moreover, the Guaymas Basin in the Gulf of California is influenced by hydrothermal activity (e.g. Von Damm, 1990). These $bSiO_2$-rich sediments are thus ideal for dedicated studies of early diagenesis under the influence of different thermal and redox conditions. We investigated the processes controlling Si isotope fractionation during early diagenesis based on pore fluid and $bSiO_2$ data from three fundamentally different environmental settings within the Guaymas Basin including the deep basin, a hydrothermal site, and a site within the Oxygen Minimum Zone (OMZ) on the slope of the Guaymas

Basin (Fig. 1). In addition, the Si isotope composition of the water column, bottom waters, and hydrothermal fluids was determined. A numerical transport-reaction model was applied to the OMZ setting to constrain marine weathering processes and to compare the results to the Peruvian margin. The aim of this study was to constrain the factors controlling Si isotope fractionation during early diagenesis and to identify processes influencing $bSiO_2$ dissolution and authigenic silicate precipitation.

2. GEOLOGICAL SETTING, SAMPLING, AND METHODS

2.1 Geological setting

The Guaymas Basin in the Gulf of California is a currently opening continental rifting environment with two graben systems (northern and southern trough), which are offset by a transform fault and reaches spreading rates of up to 6 cm yr^{-1} (Calvert, 1966). High biological productivity and terrigenous matter input result in high sediment accumulation rates and have produced thick sequences of organic-rich sediments (DeMaster, 1981). Siliceous sediments at the Guaymas Slope show fine laminations within the OMZ (dissolved oxygen <10 µM at ca. 500 – 900 m water depth; Campbell and Gieskes, 1984) due to the absence of burrowing organisms (Calvert, 1964). The Guaymas Basin is characterized by vigorous hydrothermal activity represented by Black Smoker type vents discovered in both the northern and southern troughs (Berndt et al., 2016; Von Damm et al., 1985). Hydrothermal plumes spread horizontally and mix with deep basin water up to 300 m above the seafloor resulting in a fraction of hydrothermal fluids of ~0.1% in the deep waters of the Guaymas Basin (Campbell and Gieskes, 1984). Hydrothermal sills and dikes intruding into the sediments were found to accelerate early diagenetic reactions (due to the released heat) and change pore fluid geochemistry significantly (Gieskes et al., 1982; Kastner and Siever, 1983; Von Damm et al., 1985; Von Damm, 1990). At present, pore fluids in surface sediments show a seawater composition (Geilert et al., 2018) and the absence of diagenetic high-temperature processes render these pore fluids suitable for studying recent early diagenetic processes.

2.2 Sampling

Sediments were sampled via multicorer (MUC) deployment during RV SONNE cruise SO241 in summer 2015 as described in detail in Geilert et al. (2018). In total, 6 stations have been investigated; 4 within the basin (termed basin sites: MUC33-11, MUC22-04, MUC23-05, MUC15-02), one in the vicinity of a hydrothermal vent field (termed hydrothermal site: MUC66-16), and one within the OMZ

(termed OMZ site: MUC29-09) (Fig. 1, Table 1). The coring locations within the basin were sampled in water depths between 1726 and 1855 m below sea level (mbsl). The hydrothermal site (MUC66-16) was sampled in 1842 mbsl and was located at a distance of ~500 m from the active hydrothermal mound described by Berndt et al. (2016). The OMZ site (MUC29-09) was sampled on the Guaymas Basin slope of the Mexican mainland in 665 mbsl.

After core retrieval, bottom water above the sediment was sampled and filtered immediately using 0.2 µm cellulose acetate membrane filters. Bottom water from MUC22-04 may have been contaminated with surface waters during core retrieval as indicated by Si and Mn concentrations (53.8 µM and 0.05 µM, respectively) lower than at the remaining sites within the deep basin, which show distinct anomalies caused by mixing with hydrothermal plume fluids (e.g. MUC15-02: Si = 177.8 µM and Mn = 0.34 µM). Processing of sediments was conducted in a cool laboratory in an argon-flushed glove bag immediately after core retrieval. Sampling intervals were 1-5 cm with the highest resolution close to the sediment surface and increasing distance downcore. Pore fluids were separated from sediments by centrifugation (20 min at 4500 rpm) and subsequently filtered (0.2µm cellulose acetate membrane filters) for further analyses.

Water column samples were taken using a video-guided Niskin Water sampler CTD-Rosette System. Water samples were taken in the basin above MUC15-02 at 1844 mbsl (VCTD02), within the hydrothermal plume between 1781 and 1800 mbsl (VCTD06 and 09) above the Black Smoker mound as described in Berndt et al. (2016), and above the OMZ site (MUC29-09) at 586 mbsl (Fig. 1).

2.3 $bSiO_2$ separation and digestion

The $bSiO_2$ mass fractions of sediment samples were determined using an automated leaching method following Müller and Schneider (1993) at GEOMAR Helmholtz-Centre for Ocean Research Kiel. The sample material was treated with 1M NaOH at 85°C to extract the opal fraction. The increase in dissolved Si was monitored and evaluated using a method described by DeMaster (1981). The precision of the mass fraction determination was 5 to 10% (1SD). The $bSiO_2$ was separated from the sediment for Si isotope analyses following the method of Morley et al. (2004). About 500 mg of a freeze-dried sediment sample was transferred into a centrifuge tube. Organic matter and carbonate material was removed by adding H_2O_2 (Suprapur) and HCl, respectively. Clay particles (grain size <2µm) were separated from the remaining sediment by the Atterberg method following Stoke's law (Müller, 1967). The remaining sediment ($bSiO_2$ and heavy minerals) was sieved using a 5 µm-sieve and subsequently separated from the remaining detritus using heavy liquid separation (sodium-polytungstate solution). The heavy liquid purification method was repeated until clean, examined via

light microscopy, $bSiO_2$ samples (>95%) were obtained. Light microscopy revealed that the $bSiO_2$ fraction essentially consisted of diatoms and only traces of radiolarians and sponges were present (<5%). The $bSiO_2$ samples were stored in Milli-Q water (MQ water). The $bSiO_2$ sample of the OMZ site stems from a nearby gravity core (GC07), which is described in detail in Geilert et al. (2018). The $bSiO_2$ samples were dissolved following a method by Reynolds et al. (2008). Aliquots of the cleaned $bSiO_2$ samples were transferred into Teflon vials and dried on a hot plate. Drying of the samples was shown by Ehlert et al. (2012) to have no effect the Si isotope composition of the samples. Subsequently, 1 ml of 0.1 M NaOH was added and the samples were placed on a hot plate at 130°C for 24 hours. After sample digestion, the supernatant and residue (undissolved traces of radiolarians and sponges) were separated via centrifugation. The supernatant was treated with 200 µl H_2O_2 (Suprapur) in order to remove remaining organic matter and then dried and re-dissolved in 1 ml 0.1 M NaOH at 130°C for 24 hours. After the digestion procedure, the samples were diluted with MQ water and neutralized with 1 M HCl.

2.4 XRD measurements

X-ray diffraction analyses of the dried clay samples were performed at the Central Laboratory for Crystallography and Applied Material Science, ZEKAM, dept. of Geosciences, University Bremen, using a Philips X'Pert Pro multipurpose diffractometer. The diffractometer was equipped with a Cu-tube, a fixed divergent slit of $\frac{1}{4}°$, a secondary Ni filter, and a X'Celerator detector system. A continuous scan from 3 to 85° 2θ was applied for the measurements with a calculated step size of 0.016° 2θ (calculated time per step was 50 seconds). Quantification of mineral phases were based on the Philips software X'Pert High Score™, the freely available X-ray diffraction software MacDiff 4.25 (Petschick et al., 1996), and the QUAX full-pattern method after Vogt et al. (2002). The standard deviation is ±1-3% for well crystallized minerals (see also Vogt et al., 2002) and ±5% for the remaining mineral phases.

2.5 Geochemical analyses of fluid and solid phases

Analyses of major and trace element concentrations of pore fluids from the basin sites and the hydrothermal site as well as the water column are described in Geilert et al. (2018). OMZ site pore fluids were treated in the same way. In brief, the pore fluids were analysed onboard by photometry (NH_4) and on shore for dissolved anions (Cl) and cations (Si, K, Na, Mg) using ion chromatography (IC, METROHM 761 Compact, conductivity mode) and inductively coupled plasma optical emission spectrometry (ICP-OES, VARIAN 720-ES), respectively. Analytical precision was constrained using the

IAPSO seawater standard for all chemical analyses (Gieskes et al., 1991) and was found to be <1% for Cl, <2% for K, Na, Mg, and <5% for Si.

Freeze dried and ground sediment samples were digested in HF (40% Suprapur), HNO_3 (Suprapur), and $HClO_4$ (60% p.a.) for major element analyses. The accuracy of the method was tested by method blanks and the reference standards SDO-1 (Devonian Ohio Shale, USGS) and MESS-3 (Marine Sediment Reference Material, Canadian Research Council). The digested samples were measured for their K and Al contents by ICP-OES (VARIAN 720-ES) and reproducibility was ≤5%. Total carbon (TC) and total organic carbon (TOC) were measured in freeze-dried and ground sediment samples by flash combustion using the Carlo Erba Element Analyzer (NA-1500). Carbonate carbon ($CaCO_3$) was calculated by subtracting TOC from TC.

The digested $bSiO_2$ samples were analyzed for their Al and Si contents using the Agilent 7500 series quadrupole ICPMS at GEOMAR to provide information about potential clay contamination of the separated $bSiO_2$ fraction (Shemesh et al., 1988), whereby Al/Si ratios below 50 mM/M are considered as negligible clay contamination (van Bennekom et al., 1988; Hurd, 1973). Al/Si ratios in the studied $bSiO_2$ ranged between 15 and 39 mM/M, with three exceptions in MUC22-04, MUC15-02, and MUC66-16 yielding Al/Si ratios of 71 mM/M, 57 mM/M, 50 mM/M, respectively. However, all $\delta^{30}Si_{bSiO2}$ values agreed well with surrounding $\delta^{30}Si_{bSiO2}$ values and clay contamination is thus considered unimportant. All other $bSiO_2$ samples are considered clay-free.

2.6 Sample purification and Si isotope measurements

Fluid and digested $bSiO_2$ samples were prepared for Si isotope measurements following the purification method of Georg et al. (2006b). The concentration of the samples was adjusted and loaded (1 ml with ~64 µM Si) onto 1 ml pre-cleaned cation-exchange resin (Biorad AG50 W-X8) and subsequently eluted with 2 ml MQ water. Matrix effects originating from dissolved organic compounds and anions, which cannot be separated by this purification method, have previously been found to potentially influence Si isotope measurements (van den Boorn et al., 2009; Hughes et al., 2011). However, no influence of the matrix effects on pore fluid Si isotope measurements has been found during our measurements following several tests described in Ehlert et al. (2016). Briefly, Ehlert et al. (2016) removed organic compounds by H_2O_2 and SO_4 by Ba addition yielding $\delta^{30}Si$ values identical to untreated samples, within error. Therefore, our samples were not treated with H_2O_2 or Ba before sample purification and Si isotope measurements.

Si isotope samples were measured in medium resolution on a NuPlasma MC-ICPMS (Nu InstrumentsTM, Wrexham, UK) at GEOMAR using the Cetac Aridus II desolvator. Sample Si concentrations of about 21 µM resulted in a ^{28}Si intensity of 3 to 4 V. The MQ blank was ≤ 3mV, resulting in a blank to signal ratio <0.1 %. The measurements were performed using the standard-sample bracketing method to account for mass bias drifts of the instrument (Albarède et al., 2004). Si isotopes are reported in the $\delta^{30}Si$ notation, representing the deviation of the sample $^{30}Si/^{28}Si$ from that of the international Si standard NBS28 in permil (‰). Long-term $\delta^{30}Si$ values of the reference materials Big Batch (-10.6±0.2‰; 2SD; n=49), IRMM018 (-1.5±0.2‰; 2SD; n=48), Diatomite (+1.3±0.2‰; 2SD; n=44), and BHVO-2 (-0.3±0.2‰; 2SD; n=13) are in good agreement with $\delta^{30}Si$ values in the literature (e.g. Reynolds et al., 2007; Zambardi and Poitrasson, 2011). The seawater inter-calibration standard Aloha (1000 m) resulted in +1.3±0.2‰ (2SD; n=8) in very good agreement to Grasse et al. (2017). Additionally, two in-house matrix standards have been measured. The pore fluid matrix standard yielded an average $\delta^{30}Si$ value of +1.3±0.2‰ (2SD; n=17) and the diatom matrix standard (E. rex) -1.0±0.2‰ (2SD; n=22), which agrees well with earlier reported values (Ehlert et al., 2016). All samples were measured 2-4 times on different days and the resulting $\delta^{30}Si$ values have uncertainties between 0.1 and 0.4‰ (2SD, Table 1). The $\delta^{30}Si$ values of pore fluids, $bSiO_2$, and bottom water are given as $\delta^{30}Si_{pf}$, $\delta^{30}Si_{bSiO2}$, and $\delta^{30}Si_{bw}$, respectively. Error bars in the figures indicate the uncertainty of the individual sample measurements (two standard deviation, 2SD).

2.7 Numerical model

A numerical reactive-transport model was applied to simulate Si turnover within OMZ site sediments. The model was based on a previously published Si isotope model (Ehlert et al., 2016) and was extended to consider the dissolution of additional phases. A detailed description of the model can be found in the supplementary information.

2.8 Calculation of the amount of terrigenous material and mass accumulation rate

The amount of terrigenous material (%) for the Guaymas Basin was calculated as the total mass subtracted by the carbonate content ($CaCO_3$), the organic matter content (OC), and the $bSiO_2$ content (Sayles et al., 2001):

$$\text{Terrigenous material} = 100 - (CaCO_3 + OC + bSiO_2) \quad (1)$$

The mass accumulation rate (MAR) was calculated as

$$MAR = S*d*(1-\Phi) \quad (2)$$

with S the sedimentation rate as 0.18 cm yr^{-1} (Thunell et al., 1994) and d the bulk dry density as 2.5 g cm^{-3}. The porosity (Φ) was taken at the deepest part of the core with 0.925.

3. RESULTS

3.1 Water chemistry and sediment composition

All water column, pore fluid, and hydrothermal Si concentration data, $bSiO_2$ weight fractions as well as Si isotope values are reported in Tables 1 and 2. A detailed description of the water column properties, pore fluids, and hydrothermal fluid chemistry can be found in Berndt et al. (2016) and Geilert et al. (2018). Pore fluids predominantly show a seawater composition at all sampling sites and are not influenced by high temperature processes related to sill intrusions or mixing with hydrothermal fluids. Pore fluid geochemistry of major elements in the OMZ resembles that of the remaining sampling sites with the exception of a strong enrichment in NH_4 (Table S1 and Geilert et al., 2018) as well as high Fe and low Mn concentrations (Scholz et al., 2019). The porosity corrected K (see supplement) and Al contents in the sediments ranged between 0.9 and 21.2 wt% and 2.9 and 66.6 wt%, respectively (Table 1). The TOC contents ranged between 0.3 and 7.8 % and are shown in Table S1.

3.2 Bottom water, water column, and hydrothermal fluid Si concentrations and $\delta^{30}Si$ values

The bottom water Si concentration ranged between 173 and 254 µM for all basin sites and the hydrothermal site (between 1726 and 1855 mbsl) with the exception of MUC22-04, where Si concentrations were as low as 54 µM (possible surface water contamination, see section 2.2 and Table 1). The bottom water $\delta^{30}Si_{bw}$ signatures ranged between +1.5‰ and +2.0‰ for all basin sites and the hydrothermal site and overlap within error (average $\delta^{30}Si_{bw}$: +1.8±0.2‰, 1SD; highest $\delta^{30}Si_{bw}$ for surface contaminated sample (MUC22-04)). Bottom water Si concentration for the OMZ site was 31 µM (665m water depth). The bottom water within the OMZ site had a distinctly lower $\delta^{30}Si_{bw}$ value of +0.8‰. Here, a potential contamination with surface waters can be excluded given that they are characterized by high $\delta^{30}Si$ values (from 1.7 to 4.4‰; Ehlert et al., 2012; Grasse et al., 2013), due to the preferential biological uptake of ^{28}Si (De La Rocha et al., 1997).

The basin water (VCTD02), which was sampled about 1 m above the seafloor, had a Si concentration of 163 µM and a $\delta^{30}Si_{deepBasin}$ value of +1.5‰. Hydrothermal plume Si concentrations ranged between 253 and 690 µM and $\delta^{30}Si$ values ranged from +0.7‰ (VCTD09-06) to +1.4‰ (VCTD06-06). The water column within the OMZ (586 mbsl) had a Si concentration of 78 µM and a $\delta^{30}Si_{OMZ}$ value of +1.5‰ (Table 2).

3.3 Pore fluid Si concentration and $\delta^{30}Si_{pf}$ values

Pore fluid Si concentrations generally increased asymptotically with depth from bottom water values until reaching maximum average concentrations between 605 and 864 µM Si (Table 1, Fig. 2). For the basin sites MUC33-11 and MUC15-02 as well as the OMZ site the Si concentrations asymptotically increased until average values of 742 (≥8 cm below seafloor (cmbsf)), 729 (≥9 cmbsf), and 765 (≥9 cmbsf) µM were reached, respectively. Hydrothermal site Si concentrations were higher and increased to 864 µM (≥4.5 cmbsf). MUC22-04 and MUC23-05 Si concentrations initially increased to values of on average 605 µM (5.5 - 11 cmbsf) and 735 µM (3.5 - 9 cmbsf) and then decreased again to 364 µM (26 cmbsf) and 640 µM (22 cmbsf), respectively.

Pore fluid $\delta^{30}Si_{pf}$ values for all basin sites ranged from +0.9‰ to +1.5‰ (Table 1, Fig. 2), which is lower than the respective bottom water $\delta^{30}Si_{BW}$ values ($\delta^{30}Si_{BW}$ from +1.6‰ to +2.0‰). The decrease in Si concentration at MUC22-04 and MUC23-05 below 13 cmbsf and 11 cm cmbsf, respectively, is not reflected in a significant change in $\delta^{30}Si_{pf}$. The hydrothermal site showed the highest $\delta^{30}Si_{pf}$ values ranging from +1.8‰ and +2.2‰, which is higher than the bottom water $\delta^{30}Si_{BW}$ (+1.5‰). In contrast, the OMZ site had the lowest $\delta^{30}Si_{pf}$ values between -0.5‰ and +0.8‰, which was also characterized by very low $\delta^{30}Si_{bw}$ (+0.8‰; Table 1).

3.4 $bSiO_2$ content and $\delta^{30}Si_{bSiO2}$ values

The $bSiO_2$ content of the sediments (Table 1, Fig. 2) varied between 4.7 wt% and 47.6 wt%. Lowest contents were present at the basin site MUC22-04 (7.6 -13.1 wt%) and the hydrothermal site (4.7 - 14.6 wt%). The remaining sampling sites showed higher $bSiO_2$ contents of on average 23±7 wt% (1SD). The $\delta^{30}Si_{bSiO2}$ signatures ranged between +0.4‰ and +1.0‰ and did not vary systematically with depth or sampling site within error. The small variability in $\delta^{30}Si_{bSiO2}$ signatures most likely stems from natural variability within the Guaymas Basin.

3.5 XRD results of the clay fraction

The main silicate mineral phases of all samples were phyllosilicates (16-59 wt%), primary silicates (quartz, plagioclase, potassium feldspar; 15-38 wt%), and amorphous SiO_2 (4-43 wt% including abiogenic and biogenic opal) (Table S2). The phyllosilicates were mainly composed of variable fractions of smectite, illite, montmorillonite, and kaolinite. Apart from silicate minerals, minor amounts of Fe-(hydr-)oxides (≤10 wt%, most between 2 and 3 wt%), pyroxenes (≤8 wt%), and carbonates (≤6 wt%) were present. Biogenic opal fragments were identified via light microscopy to be the dominating amorphous silicate phase at all sites besides the hydrothermal site and MUC23-05 in the basin basin. At the hydrothermal site, the abiogenic amorphous silica fraction was the dominating silica phase in the uppermost and lowermost core sections with only minor occurrences of biogenic opal fragments. Abiogenic amorphous silica was also found in the uppermost and lowermost core sections of MUC23-05.

4. DISCUSSION

Pore fluid Si concentration and $\delta^{30}Si_{pf}$ signatures vary significantly between sampling sites and appear to depend strongly on ambient conditions. The Si concentration and isotope compositions are proposed to be affected by dissolution of $bSiO_2$, the dissolution of terrigenous phases, and the formation of authigenic aluminosilicates; the latter process is defined as reverse weathering. Dissolution of $bSiO_2$ is most effective in the reactive surface layer (≤ 10 cmbsf) where the degree of Si undersaturation is highest. When Si is released into solution via $bSiO_2$ dissolution, certain amounts of Si re-precipitate as authigenic aluminosilicates as a function of the availability of reactive metals, made available by dissolution of terrigenous material (e.g. Michalopoulos and Aller, 1995; Van Cappellen and Qiu, 1997a,b; Loucaides et al., 2010). In the course of this process authigenic silicate precipitation induces $\delta^{30}Si$ fractionation, whereby the ^{28}Si is preferentially incorporated into the solid phase, enriching the remaining fluid in ^{30}Si (Ehlert et al., 2016). In the following sections, the processes during early diagenesis influencing pore fluid $\delta^{30}Si_{pf}$ signatures under different ambient conditions are discussed. For the OMZ site, we quantify these processes using a reactive transport model and compare the results to the only other OMZ site where pore fluid $\delta^{30}Si_{pf}$ data is available, the Peruvian margin.

4.1. Influences on $\delta^{30}Si_{pf}$ due to source mixing

In the open ocean, a strong correlation between the inverse Si concentration (1/Si) and Si isotope composition in intermediate and deep waters exists, showing low $\delta^{30}Si$ values with high Si

concentrations and can be used to identify water mass mixing between two endmembers with distinct Si characteristics (e.g. de Souza et al., 2012). Here, we use the two endmember mixing Eq. (3) to calculate the mixing between the deep water column and fluids originating from $bSiO_2$ dissolution according to

$$\delta^{30}Si_{mix} = \frac{(\delta^{30}Si_{\text{water column}} * [Si]_{\text{water column}} * f) + (\delta^{30}Si_{bSiO2} * [Si]_{bSiO2} * (1-f))}{([Si]_{\text{water column}} * f) + ([Si]_{bSiO2} * (1-f))} \quad (3)$$

with $\delta^{30}Si_{\text{water column}}$ and $[Si]_{\text{water column}}$ as the respective water column Si isotope composition and concentration (Table 2) and $\delta^{30}Si_{bSiO2}$ as the average $bSiO_2$ value (+0.8‰) of all sites. The equilibrium concentration in respect to $bSiO_2$ dissolution was derived from an experimental study by Van Cappellen and Qiu (1997a) with $[Si]_{bSiO2}$ = 900µM. Mixing fractions are represented by *f*, varied over 100% water column and 0% fluids affected by $bSiO_2$ dissolution and vice versa.

Pore fluid $\delta^{30}Si_{pf}$ values of all sites deviate from mixing curves between the deep water column and fluids originating from $bSiO_2$ dissolution and are obviously affected by additional processes (Fig. 3). Si isotope fractionation during $bSiO_2$ dissolution is not well constrained and ranges between -0.55‰ and 0‰, while most studies argue against a significant isotope effect (Demarest et al., 2009; Egan et al., 2012; Wetzel et al., 2014). Therefore, we will also exclude Si isotope fractionation in dependence of $bSiO_2$ dissolution as a process affecting pore fluid $\delta^{30}Si_{pf}$ values. The $\delta^{30}Si_{pf}$ values of the basin sites and hydrothermal site are higher (+0.9‰ to +2.2‰) compared to the respective mixing curves, while $\delta^{30}Si_{pf}$ values of the OMZ site are lower (-0.5‰ to +0.8‰). While a shift to lower $\delta^{30}Si_{pf}$ values points to dissolution of an isotopically light phase, higher $\delta^{30}Si_{pf}$ values indicate that precipitation processes are important, given that the light Si isotope is preferentially incorporated in authigenic secondary phases (Georg et al., 2009). This indicates that processes governing the pore fluid Si isotope composition differ significantly between the individual sites.

4.2. Influences on $\delta^{30}Si_{pf}$ from terrigenous and biogenic material

The terrigenous/$bSiO_2$ ratio was found to be the main mechanism controlling asymptotic pore fluid Si concentration and the benthic Si flux (Van Cappellen and Qiu, 1997a, b). Maximum Si concentrations were reached asymptotically at four out of six sampling sites (Fig. 2). Two sites within the basin (MUC22-04 and MUC23-05) show lower Si concentrations in the deep core sections (Fig. 2), which are most likely related to the decrease of reactive silica with depth, caused by the formation of less soluble silica phases (Van Cappellen and Qiu, 1997a). At these sites, the asymptotic Si concentration

is defined as the maximum concentration values in the center of the core. The amount of terrigenous material for the Guaymas Basin was calculated according to Eq. (1) and accounts for 75%.

Asymptotic Si concentrations plotted against the terrigenous/$bSiO_2$ ratio fall on the global trend except for the hydrothermal site (Fig. 4a). Here, high geothermal gradients are likely responsible for the higher Si concentrations with respect to the global trend (see also section 4.3.2). In contrast to the asymptotic Si concentration, no strong correlation of the pore fluid $\delta^{30}Si_{pf}$ values with the terrigenous/$bSiO_2$ ratio exists (Fig. 4b). In order to identify processes responsible for the different pore fluid $\delta^{30}Si_{pf}$ values and to facilitate comparison between the three settings within the Guaymas Basin, only average $\delta^{30}Si_{pf}$ values will be discussed in the following.

Average $\delta^{30}Si_{pf}$ values show distinct variations between the individual settings. The $\delta^{30}Si_{pf}$ values of the OMZ site are lower (0.0±0.5‰, 1SD, n = 6) than those of the basin sites (+1.2±0.1‰, 1SD, n = 17) and the hydrothermal site, which shows the highest $\delta^{30}Si_{pf}$ values (+2.0±0.2‰, 1SD, n = 3). The homogeneity of the individual $\delta^{30}Si_{pf}$ profiles indicates that possible effects of bioirrigation at the basin sites and hydrothermal site are quickly compensated by isotopic exchange. Similarly, bioturbation has also little impact on the sediment composition given the the homogeneity of the $bSiO_2$ content profiles with depth (Fig. 2).

4.3 Influence of the ambient environmental conditions on the $\delta^{30}Si_{pf}$ values

4.3.1 Basin sites

Pore fluid $\delta^{30}Si_{pf}$ values of the basin sites deviate from the mixing curve between the deep water column and fluids originating from $bSiO_2$ dissolution and are shifted to higher values (+1.2±0.1‰; Fig. 3). This shift to higher $\delta^{30}Si_{pf}$ values can be explained by Si re-precipitation as authigenic aluminosilicates, which preferentially incorporate the light ^{28}Si isotope (Fig. 5a). Alteration of terrigenous material leads to mobilization and re-precipitation of Al and the uptake of K from seawater in the authigenic phase (Michalopoulos and Aller, 2004). The sedimentary K/Al ratio can thus be used to detect these early diagenetic reactions in addition to pore fluid $\delta^{30}Si_{pf}$ values. Authigenic aluminosilicates formed during alteration of terrigenous material were found to have K/Al ratios of 0.32 (Michalopoulos and Aller, 2004), which is higher than the pristine K/Al ratio of terrigenous material carried by rivers (K/Al = 0.19; Viers et al., 2009). The average K/Al ratio of the basin sites is 0.34±0.01 (1SD), which is in the same range as K/Al ratios indicative of authigenic aluminosilicate formation (Michalopoulos and Aller, 2004). Thus, at basin sites both K/Al ratios and

451 $\delta^{30}Si_{pf}$ values are in agreement to recognize $bSiO_2$ dissolution followed by authigenic clay formation
452 as significant processes taking place.
453
454 4.3.2 Hydrothermal site
455
456 The $\delta^{30}Si_{pf}$ values from the hydrothermal site are higher (+2.0±0.2‰) than the mixing curve between
457 the deep water column and fluids originating from $bSiO_2$ dissolution and also much higher than pore
458 fluid $\delta^{30}Si_{pf}$ values from the basin (Fig. 3, 5a). The high $\delta^{30}Si_{pf}$ values indicate that precipitation plays a
459 significant role at this site. Sedimentary K/Al ratios are equivalent to basin values (K/Al = 0.34) and
460 thus show the formation of authigenic aluminosilicates. Consequently, the higher pore fluid $\delta^{30}Si_{pf}$
461 values compared to the basin sites can either be explained by a different Si isotope fractionation
462 factor or by the precipitation of additional silica phases. The hydrothermal site is located in close
463 proximity to a hydrothermal vent field and hydrothermal deposits are mainly composed of Fe-
464 sulfides (Berndt et al., 2016), while nearby sediments are dominated by amorphous silica, quartz, and
465 Fe-Si silicates (e.g. ferrosilite, fayalite) (Kastner, 1982; Von Damm et al., 1985). Si adsorption to iron
466 (oxyhydr)oxide and incorporation into Fe-Si gels can create substantial Si isotope fractionation with
467 ^{28}Si being preferentially enriched in the solid phase (Delstanche et al., 2009; Zheng et al., 2016). Pore
468 fluids show high Fe^{2+} concentrations (up to 190 µM; Scholz et al., 2019) and the precipitation of Fe-Si
469 silicates is thus likely, shifting pore fluid $\delta^{30}Si_{pf}$ to the observed high values. Saturation indices
470 calculated based on the program PHREEQC (Parkhurst and Appelo, 1999) indicate that quartz is
471 supersaturated and amorphous silica is close to saturation at about > 6cmbsf (Fig. S1). Due to the
472 dynamics of hydrothermal systems, this can be subject to changes and supersaturation of amorphous
473 silica is likely to be obtained occasionally, due to the ascent of Si enriched fluids from greater depth.
474 Gieskes et al. (1988) reported on amorphous silica cement in the hydrothermally-influenced
475 sediments of the Guaymas Basin, which is supported by findings of this study and likely explains the
476 high amorphous SiO_2 contents identified by XRD (~35 wt%; see Sect. 3.5; Table S2). In the Guaymas
477 Basin, high thermal gradients (up to 11 K m^{-1}; Geilert et al., 2018) caused by igneous sill intrusions
478 near the active spreading center significantly influence diagenetic reactions at depth and accelerate
479 Si dissolution and precipitation (Fig. 5a) (e.g. Kastner and Siever, 1983). This can also explain the high
480 pore fluid $\delta^{30}Si_{pf}$ values, given that deep Si saturated fluids ascent and Si precipitates, likely along
481 with Fe, over a large temperature range, whereby lower temperatures are associated with larger Si
482 isotope fractionation shifting pore fluid $\delta^{30}Si_{pf}$ to the observed high values (Geilert et al., 2014; Zheng
483 et al., 2016).
484
485 4.3.3 OMZ site

At the OMZ site, the $\delta^{30}Si_{pf}$ values are significantly lower (on average 0.0±0.5‰) than the water column $\delta^{30}Si_{water\ column}$ value (+1.5±0.2‰) and also lower than the $\delta^{30}Si_{bSiO2}$ value (+0.8‰) (Fig. 2, 3). Interestingly, the only other $\delta^{30}Si_{pf}$ values from an OMZ were obtained at the Peruvian margin (Ehlert et al., 2016), where the $\delta^{30}Si_{pf}$ values in the upper 10 cmbsf are slightly higher than the water column $\delta^{30}Si_{bw}$ values (+1.8‰ and +1.5‰, respectively). As Ehlert et al. (2016) concluded, the Peruvian $\delta^{30}Si_{pf}$ values are influenced by $bSiO_2$ dissolution and precipitation of authigenic aluminosilicates, the latter process shifting pore fluid $\delta^{30}Si_{pf}$ to values higher than those of the water column. Consequently, in order to explain the extremely low $\delta^{30}Si_{pf}$ values at the Guaymas Basin OMZ, an additional process must occur. We hypothesize that a phase enriched in ^{28}Si needs to dissolve in order to shift the pore fluid $\delta^{30}Si_{pf}$ values and this phase might be 1) iron (oxyhydr)oxides with adsorbed ^{28}Si or 2) terrestrial clays.

Silicon exhibits a strong affinity to iron (oxyhydr)oxides (see also section 4.3.2; Davis et al., 2002) and Si isotopes fractionate significantly during Si adsorption and co-precipitation (Delstanche et al., 2009; Zheng et al., 2016). Dissolved Fe^{2+} in pore fluids can be transferred across the sediment-water interface via diffusion and re-precipitates as iron (oxyhydr)oxides, where it subsequently dissolves again in the reducing sediment. This process can repeat, resulting in multiple cycles of Fe dissolution and re-precipitation on the Guaymas Basin slope (Scholz et al., 2019). We hypothesize that the light ^{28}Si adsorbs to iron (oxyhydr)oxides in the water column and that upon reductive dissolution of Fe minerals in the surface sediment, the light ^{28}Si isotope is re-released into the pore fluids, adding to the observed low $\delta^{30}Si_{pf}$ values. However, the quantification of this Fe-Si shuttle and the contribution to the low $\delta^{30}Si_{pf}$ values in OMZ pore fluids remains difficult given that Fe undergoes multiple cycles of dissolution and re-precipitation. Furthermore, the exact process of complexation, Si isotope fractionation, and co-precipitation is unknown and requires further investigations (see also Fig. S3). We can only speculate that the transport of ^{28}Si via the Fe-Si shuttle is only of minor importance given that the MAR of $bSiO_2$ and terrigenous material are dominating the Si supply to Guaymas OMZ sediments (Calvert, 1966; DeMaster, 1981).

The low $\delta^{30}Si_{pf}$ values can also be explained by dissolution of terrigenous clay particles, which are generally enriched in ^{28}Si, showing a large range in $\delta^{30}Si$ with the majority between -3‰ to 0‰ (Frings et al., 2016 and references therein). Primary minerals like feldspars or olivine, which are generally considered to control marine weathering reactions (e.g. Wallmann et al., 2008) have higher $\delta^{30}Si$ values (e.g. feldspars with -0.15‰; Georg et al., 2009) and their dissolution alone cannot create the low pore fluid $\delta^{30}Si_{pf}$ values (see supplement and Fig. S6). Clays are usually considered to be the

stable end product of silicate weathering. However, fine clay particles and highly reactive surface sites of clays such as montmorillonite, smectite and illite may dissolve in natural waters (Cappelli et al., 2018; Golubev et al., 2006; Köhler et al., 2005). The dissolution is promoted by organic ligands and the reduction of structural iron of clay minerals under reducing conditions (Anderson and Raiswell, 2004). Humic substances that are abundant in OMZ sediments enriched in organic matter may catalyze the microbial reduction of structural iron in clays (Lovley et al., 1998) and their dissolution (Liu et al., 2017). Clays are abundant in OMZ sediments, given that fine-grained terrigenous material is transported downslope from the shelf to the basin (Scholz et al., 2019). Furthermore, the microbial oxidation of ferrous Fe in these fine-grained silicate minerals and its subsequent conversion to reactive iron minerals was also found to contribute to the Fe cycling at the Guaymas Basin slope (Scholz et al., 2019).

In order to constrain the possibility of terrigenous clay dissolution and the related shift to low $\delta^{30}Si_{pf}$ values in the Guaymas OMZ a reactive transport model was applied, based on our previously published $\delta^{30}Si$ model (Ehlert et al., 2016). The data obtained at the Guaymas OMZ were used to model the turnover of Si in these sediments and the previously published model extended to consider additional processes (Fig. 6). A full description of the model is presented in the supplementary information. The model was fit to dissolved Si concentrations and $\delta^{30}Si$ values measured in pore fluids and biogenic opal and K/Al ratios determined in the solid phase (Fig. 6). High rates of terrigenous clay dissolution were applied at the sediment surface to reproduce the observed minima in $\delta^{30}Si_{pf}$ pore fluid values and K/Al ratios in a model run best fitting our data set (Fig. 6, best fit). Since the terrigenous phases deposited at the sediment surface contain potassium (K_{terr} = 1.7 wt%, K/Al = 0.19; Viers et al., 2009) and are depleted in ^{30}Si (clay $\delta^{30}Si$ (late stage weathering product) = -2‰; Opfergelt et al., 2010), the dissolution of these phases induces a decline in pore fluid $\delta^{30}Si$ and solid phase K/Al (supplementary information). The precipitation of authigenic phases that are depleted in ^{30}Si (Si isotope fractionation: $\Delta^{30}Si_{au}$ = -2‰; Ehlert et al., 2016) and characterized by high K contents (K/Al = 0.32; Michalopoulos and Aller, 2004) induces a down-core increase in pore fluid $\delta^{30}Si_{pf}$ and solid phase K/Al below the surface minimum. Consequently, terrigenous clay dissolution under the reducing conditions of the OMZ and subsequent authigenic aluminosilicate precipitation can explain the low $\delta^{30}Si_{pf}$ values detected in Guaymas OMZ pore fluids (Fig. 5). However, our model results should be regarded with caution because we applied strongly simplifying assumptions (e.g. steady state, simple rate laws). Moreover, our estimates of solid phase reactivity and isotopic composition are preliminary and not supported by independent data.

Additional simulations were conducted to investigate how the solid phase and pore fluid composition is affected by the dissolution of terrigenous clay phases and the precipitation of authigenic phases (Fig. 6) and how varying $\delta^{30}Si$ values of the dissolving terrigenous phase and Si isotope fractionation factors impact pore fluid $\delta^{30}Si_{pf}$ values (Fig. S6). Furthermore, varying K/Al ratios and $bSiO_2$ solubilities are tested (see supplement). The surface minima in pore fluid $\delta^{30}Si_{pf}$ and solid phase K/Al disappear when the dissolution rate is set to zero ($R_{terr} = 0$) while the ongoing precipitation of authigenic phases leads to a strong down-core increase and high values at depth that are not consistent with the data. Pore fluid $\delta^{30}Si_{pf}$ and solid phase K/Al values strongly decrease with depth when the rate of authigenic phase precipitation is set to zero ($R_{au} = 0$) such that the model yields values that are significantly lower than the measured values. Dissolved Si concentrations cannot be used to further constrain R_{terr} and R_{au} because they are largely controlled by the dissolution of biogenic opal (R_{opal}). Dissolved K concentrations show a much lower sensitivity to R_{terr} and R_{au} than solid phase K/Al ratios due to the high porosity of the OMZ sediments. Changes in dissolved K are largely eliminated by molecular diffusion that is favored by the high porosity while the effect of the solid phase reactions R_{terr} and R_{au} on the pore fluid composition is diminished by the low solid phase contents and the high background concentration of dissolved K in ambient bottom waters. However, the model runs show that the more sensitive pore fluid $\delta^{30}Si_{pf}$ and solid phase K/Al can be used to constrain the balance between the dissolution of terrigenous phases and the precipitation of authigenic phases and that both reactions are required to model the low $\delta^{30}Si_{pf}$ values measured in the Guaymas OMZ. Additionally, $\delta^{30}Si$ values for the dissolving terrigenous material higher than -2‰ cannot reproduce the measured $\delta^{30}Si$ values in the OMZ pore fluids. Only if the fractionation factor is lowered to -1‰, terrigenous material with $\delta^{30}Si$ values of -1.7‰ can produce the observed values (Fig. S6). Thus, low pore fluid $\delta^{30}Si$ values in the Guaymas OMZ can only be reproduced by dissolving terrigenous clay particles highly depleted in ^{30}Si.

The modelled Si isotope composition of the benthic flux is -0.97‰, which is lower than the $\delta^{30}Si$ value of the bottom water (+0.8‰). The higher bottom water $\delta^{30}Si$ value along with the low Si concentration (~30µM), which is lower than the ambient water column Si concentration (~80µM), indicates that a certain amount of Si must directly re-precipitate at the sediment water interface. Still the $\delta^{30}Si$ of the bottom water is lower compared to the ambient water column, showing a benthic Si flux with low $\delta^{30}Si$ values at continental margin settings, which is also in excellent agreement with previously modelled and calculated $\delta^{30}Si$ values (Ehlert et al., 2016; Grasse et al., 2016). These findings show that benthic Si fluxes at continental margins are a source of low $\delta^{30}Si$ values to the ocean and need to be taken into account in future marine Si budget models.

590 4.4 Controlling processes and the impact on the global marine Si cycle

591

592 Stable and radioactive Si isotope data revealed significant sedimentary import and export processes
593 influencing the marine Si cycle (Ehlert et al., 2013, 2016; Tréguer and De La Rocha, 2013; Grasse et
594 al., 2016; Rahman et al., 2017; Sutton et al., 2018). Diatom burial removes about 9.9 Tmol yr^{-1} Si from
595 the ocean to the sediments, however, effects of terrigenous silicate dissolution and reverse silicate
596 weathering on $bSiO_2$ burial, preservation, and the benthic Si flux (and its Si isotope composition) are
597 not well constrained (Sutton et al., 2018). It has previously been shown that silicate minerals dissolve
598 in deep methanogenic sediments where the dissolution process is favored by high CO_2 and organic
599 ligand concentrations in ambient pore fluids (Wallmann et al., 2008). Similar to chemical weathering
600 on land, the dissolution of terrigenous silicate phases in marine sediments leads to a release of
601 cations and the conversion of CO_2 into HCO_3^-. Moreover, this marine weathering process provides the
602 dissolved Al that is needed for reverse weathering reactions. Our OMZ data show for the first time
603 that marine silicate weathering (dissolution of terrigenous silicates) also occurs in OMZ surface
604 sediments where it can outpace reverse weathering (precipitation of authigenic silicates). Our study
605 indicates that ambient environmental conditions appear to significantly influence the balance
606 between marine weathering and reverse weathering and thereby the Si flux back to the ocean. Pore
607 fluid $\delta^{30}Si_{pf}$ values depend on a complex interplay between $bSiO_2$, terrigenous silicate dissolution, and
608 authigenic aluminosilicate precipitation, however, the controlling factors that determine which
609 process dominates are difficult to constrain (Fig. 5). In view of the OMZ settings (Guaymas Basin
610 versus Peruvian margin), the most pronounced difference is the MAR_{terr} which is significantly higher
611 in the Guaymas Basin (252 g m^{-2} yr^{-1}; calculated by multiplying the terrigenous content derived in Eq.
612 (1) with the MAR from Eq. (2)) than at the Peruvian margin (100 g m^{-2} yr^{-1}; MAR from Ehlert et al.,
613 2016; terrigenous content calculated after Eq. (1) with 6 wt% $bSiO_2$, 15 wt% OC, 8 wt% $CaCO_3$) (Fig.
614 5a, b). The high terrigenous detritus content is supplied via rivers in the Guaymas Basin (Calvert,
615 1966; DeMaster, 1981). In combination with the high MAR_{terr} in the Guaymas OMZ, high water/rock
616 ratios (high porosity) additionally promote dissolution processes (Fig. 5). Lower MAR_{terr} and
617 water/rock ratios found in the Peruvian upwelling margin appear to limit the dissolution rate of
618 terrigenous phases and promote authigenic aluminosilicate precipitation (Fig. 5b, c), shifting pore
619 fluid $\delta^{30}Si_{pf}$ to higher values compared to the corresponding $\delta^{30}Si_{bSiO2}$ and $\delta^{30}Si_{bw}$ values. This
620 illustrates that the pore fluid $\delta^{30}Si_{pf}$ values of apparently similar settings (e.g. OMZ sites) highly
621 depend on the ambient environmental conditions and are not easily transferable.

622

623 4.5 Hydrothermal impact on the marine Si cycle

624

Findings of this study show that additional Si sources like hydrothermal input appear to affect the oceanic $\delta^{30}Si$ values only in close vicinity to the hydrothermal fields. The $\delta^{30}Si$ values of the hydrothermal plume (+0.7 to +1.4‰) are highly diluted by seawater (≥ 94%, Table 2) and thus deviate from hydrothermal fluid $\delta^{30}Si$ values (-0.3‰; De La Rocha et al., 2000). However, the currently available data set regarding $\delta^{30}Si$ values of hydrothermal fluids is limited (two data points; De La Rocha et al., 2000), even though they are in excellent agreement with oceanic crust $\delta^{30}Si$ values (-0.29±; Savage et al., 2010), the rock through which hydrothermal fluids circulate and gain their Si isotopic signature. In our data set, no correlation exists between the $\delta^{30}Si$ values and the Si concentration of the hydrothermal plume (Fig. S2) and instead the $\delta^{30}Si$ values are predominantly controlled by Si precipitation, likely in the hydrothermal conduit during ascent or after discharge in contact with colder seawater. Temperature variations and interlinked precipitation rates were found in addition to co-precipitation with Al or Fe to cause large Si fractionation such that precipitates are enriched in ^{28}Si (Geilert et al., 2014, 2015; Oelze et al., 2015; Roerdink et al., 2015; Zheng et al., 2016). The varying impacts of these factors can also explain why the diluted hydrothermal plume $\delta^{30}Si$ values with the highest hydrothermal share (Table 2) does not show the lowest $\delta^{30}Si$ values, indicative of hydrothermal fluids, given that Si is more reactive compared to Mg, the element on which the hydrothermal share calculations are based (see supplement from Berndt et al., 2016). The large range in hydrothermal plume $\delta^{30}Si$ values, which clearly show high degrees of seawater dilution, illustrates the complexity of precipitation processes when hydrothermal fluids get in contact with cold seawater and which requires further investigations especially with respect to the impact on the global marine Si cycle.

5. CONCLUSIONS

Marine silicate weathering and reverse weathering impact the pore fluid isotopic composition of sediments and are key processes of the marine Si cycle. In the Guaymas Basin, these processes have been studied under markedly differing thermal and redox conditions. Si isotope compositions of pore fluids combined with those of biogenic silica and ambient bottom waters helped to decipher marine weathering and reverse weathering reactions, which would have remained undetected by elemental concentrations alone and highlight the importance of Si isotope studies to constrain early diagenetic reactions. Si concentrations and $\delta^{30}Si_{pf}$ signatures are the result of the interplay between silica dissolution and Si precipitation, however, the involved phases differ significantly between the study sites. Large differences in $\delta^{30}Si_{pf}$ values in a regionally constrained basin show that oxic/anoxic conditions, hydrothermal fluids, water/rock ratios and the input of terrigenous material strongly affect the pathways and turnover rates of Si in marine sediments. The light $\delta^{30}Si_{pf}$ and $\delta^{30}Si_{BW}$ values

from the Guaymas OMZ confirm earlier studies suggesting a light Si isotope value of the benthic Si flux (Ehlert et al., 2016; Grasse et al., 2016), which need to be taken into account in future oceanic mass balances of Si and in modelling studies concerning the isotopic Si cycle. Environmental settings, in particular the MARs of terrigenous material, water/rock ratios, and redox conditions appear to be the major factors controlling the balance between marine silicate weathering and reverse weathering and the Si isotope fractionation in pore fluids of marine sedimentary settings and need to be considered particularly in marine Si isotope studies.

AUTHOR CONTRIBUTION

SG, CH, MS, and FS helped sampling and processing of the samples onboard. SG, PG, and KD conducted the Si isotope measurements. SG, CE, PG, KD, FS, and MF helped interpreting the data. KW designed the reactive transport model. SG prepared the manuscript with the contribution of all authors.

COMPETING INTEREST

The authors declare that they have no conflict of interest.

ACKNOWLEDGEMENTS

This work was part of the MAKS project funded by the German Ministry of Science and Education (BMBF). We appreciate the support of the master and crew of the R/V Sonne during the SO241 cruise. We thank Regina Surberg, Bettina Domeyer, and Anke Bleyer for analytical support during the cruise and on shore. Further thanks go to Tabitha Riff, Jutta Heinze, and Tyler Goepfert. Additional support of this work was provided by EU-COST Action ES1301 "FLOWS" (www.flows-cost.eu) and the German Collaborative Research Centre (SFB) 754: Climate – Biogeochemistry Interactions in the Tropical Ocean funded by the German Science Foundation. We would also like to thank an anonymous reviewer, Jill Sutton, and Damien Cardinal for their comments and constructive reviews.

References

Abrantes, F., Lopes, C., Mix, A. and Pisias, N.: Diatoms in Southeast Pacific surface sediments reflect environmental properties, Quat. Sci. Rev., 26(1–2), 155–169,

695 doi:10.1016/j.quascirev.2006.02.022, 2007.
696 Albarède, F., Telouk, P., Blichert-Toft, J., Boyet, M., Agranier, A. and Nelson, B.: Precise and accurate
697 isotopic measurements using multiple-collector ICPMS, Geochim. Cosmochim. Acta, 68(12),
698 2725–2744, doi:10.1016/j.gca.2003.11.024, 2004.
699 Anderson, T. F. and Raiswell, R.: SOURCES AND MECHANISMS FOR THE ENRICHMENT OF HIGHLY
700 REACTIVE IRON IN EUXINIC BLACK SEA SEDIMENTS, Am. J. Sci., 304, 203–233, 2004.
701 van Bennekom, A. J., Berger, G. . W., Van Der Gaast, S. J. and De Vries, R. T. P.: PRIMARY
702 PRODUCTIVITY AND THE SILICA CYCLE IN THE SOUTHERN OCEAN (ATLANTIC SECTOR),
703 Palaeogeogr. Palaeoclim. Palaeoecol., 67, 19–30, 1988.
704 Berndt, C., Hensen, C., Mortera-Gutierrez, C., Sarkar, S., Geilert, S., Schmidt, M., Liebetrau, V., Kipfer,
705 R., Scholz, F., Doll, M., Muff, S., Karstens, J., Planke, S., Petersen, S., Böttner, C., Chi, W.-C.,
706 Moser, M., Behrendt, R., Fiskal, A., Lever, M. A., Su, C.-C., Deng, L., Brennwald, M. S. and
707 Lizarralde, D.: Rifting under steam – how rift magmatism triggers methane venting from
708 sedimentary basins, Geology, 44(9), 767–770, 2016.
709 Beucher, C. P., Brzezinski, M. A. and Jones, J. L.: Sources and biological fractionation of Silicon
710 isotopes in the Eastern Equatorial Pacific, Geochim. Cosmochim. Acta, 72(13), 3063–3073,
711 doi:10.1016/j.gca.2008.04.021, 2008.
712 Beucher, C. P., Brzezinski, M. A. and Jones, J. L.: Mechanisms controlling silicon isotope distribution in
713 the Eastern Equatorial Pacific, Geochim. Cosmochim. Acta, 75(15), 4286–4294,
714 doi:10.1016/j.gca.2011.05.024, 2011.
715 van den Boorn, S. H. J. M., Vroon, P. Z. and van Bergen, M. J.: Sulfur-induced offsets in MC-ICP-MS
716 silicon-isotope measurements, J. Anal. At. Spectrom., 24(8), 1111, doi:10.1039/b816804k,
717 2009.
718 Bruland, K. W., Rue, E. L., Smith, G. J. and DiTullio, G. R.: Iron, macronutrients and diatom blooms in
719 the Peru upwelling regime: Brown and blue waters of Peru, Mar. Chem., 93(2–4), 81–103,
720 doi:10.1016/j.marchem.2004.06.011, 2005.
721 Calvert, S. E.: Factors affecting distribution of laminated diatomaceous sediments in Gulf of
722 California, in Marine Geology of Gulf of California, edited by T. van Andel and G. G. Shor, pp.
723 311–330, Am Assoc. Petrol. Geol. Mem.3., 1964.
724 Calvert, S. E.: Accumulation of Diatomaceous Silica in the Sediments of the Gulf of California, Geol.
725 Soc. Am. Bull., 77(June), 569–596, 1966.
726 Campbell, A. C. and Gieskes, J. M.: Water column anomalies associated with hydrothermal activity in
727 the Guaymas Basin, Gulf of California Andrew C. Campbell and Joris M. Gieskes, Earth Planet.
728 Sci. Lett., 68, 57–72, 1984.
729 Van Cappellen, P. and Qiu, L. Q.: Biogenic silica dissolution in sediments of the Southern Ocean.1.

730 Solubility, Deep. Res. Part Ii-Topical Stud. Oceanogr., 44(5), 1109–1128, doi:10.1016/S0967-
731 0645(96)00113-0, 1997a.
732 Van Cappellen, P. and Qiu, L.: Biogenic silica dissolution in sediments of the Southern Ocean . II
733 Kinetics, Deep. Res. II, 44(5), 1129–1149, 1997b.
734 Cappelli, C., Yokoyama, S., Cama, J. and Huertas, F. J.: Montmorillonite dissolution kinetics:
735 Experimental and reactive transport modeling interpretation, Geochim. Cosmochim. Acta,
736 227, 96–122, 2018.
737 Cardinal, D., Alleman, L. Y., Dehairs, F., Savoye, N., Trull, T. W. and André, L.: Relevance of silicon
738 isotopes to Si-nutrient utilization and Si-source assessment in Antarctic waters, Global
739 Biogeochem. Cycles, 19(2), 1–13, doi:10.1029/2004GB002364, 2005.
740 Von Damm, K. L.: Seafloor Hydrothermal Activity: Black Smoker Chemistry And Chimneys, Annu. Rev.
741 Earth Planet. Sci., 18(1), 173–204, doi:10.1146/annurev.earth.18.1.173, 1990.
742 Von Damm, K. L., Edmond, J. M., Measures, C. I. and Grant, B.: Chemistry of submarine hydrothermal
743 solutions at Guaymas Basin, Gulf of California, Geochim. Cosmochim. Acta, 49(11), 2221–
744 2237, 1985.
745 Davis, C. C., Chen, H. W. and Edwards, M.: Modeling silica sorption to iron hydroxide, Environ. Sci.
746 Technol., 36(4), 582–587, doi:10.1021/es010996t, 2002.
747 Delstanche, S., Opfergelt, S., Cardinal, D., Elsass, F., André, L. and Delvaux, B.: Silicon isotopic
748 fractionation during adsorption of aqueous monosilicic acid onto iron oxide, Geochim.
749 Cosmochim. Acta, 73(4), 923–934, doi:10.1016/j.gca.2008.11.014, 2009.
750 Demarest, M. S., Brzezinski, M. a. and Beucher, C. P.: Fractionation of silicon isotopes during biogenic
751 silica dissolution, Geochim. Cosmochim. Acta, 73(19), 5572–5583,
752 doi:10.1016/j.gca.2009.06.019, 2009.
753 DeMaster, D. J.: The supply and accumulation of silica in the marine environment., Geochemica
754 Cosmochim. Acta, 45, 1715–1732, 1981.
755 Dixit, S., Van Cappellen, P. and van Bennekom, A. J.: Processes controllong solubility of biogenic silica
756 and pore water build-up of silicic acid in marine sediments, Mar. Chem., 73, 333–352, 2001.
757 Doering, K., Ehlert, C., Grasse, P., Crosta, X., Fleury, S., Frank, M. and Schneider, R.: Differences
758 between mono-generic and mixed diatom silicon isotope compositions trace present and
759 past nutrient utilisation off Peru, Geochim. Cosmochim. Acta, 177, 30–47,
760 doi:10.1016/j.gca.2015.12.029, 2016.
761 Egan, K. E., Rickaby, R. E. M., Leng, M. J., Hendry, K. R., Hermoso, M., Sloane, H. J., Bostock, H. and
762 Halliday, A. N.: Diatom silicon isotopes as a proxy for silicic acid utilisation : A Southern Ocean
763 core top calibration, Geochim. Cosmochim. Acta, 96, 174–192,
764 doi:10.1016/j.gca.2012.08.002, 2012.

765 Ehlert, C., Grasse, P., Mollier-Vogel, E., Böschen, T., Franz, J., de Souza, G. F., Reynolds, B. C.,
766 Stramma, L. and Frank, M.: Factors controlling the silicon isotope distribution in waters and
767 surface sediments of the Peruvian coastal upwelling, Geochim. Cosmochim. Acta, 99, 128–
768 145, doi:10.1016/j.gca.2012.09.038, 2012.
769 Ehlert, C., Grasse, P. and Frank, M.: Changes in silicate utilisation and upwelling intensity off Peru
770 since the Last Glacial Maximum - insights from silicon and neodymium isotopes, Quat. Sci.
771 Rev., 72, 18–35, doi:10.1016/j.quascirev.2013.04.013, 2013.
772 Ehlert, C., Doering, K., Wallmann, K., Scholz, F., Sommer, S., Grasse, P., Geilert, S. and Frank, M.:
773 Stable silicon isotope signatures of marine pore waters – Biogenic opal dissolution versus
774 authigenic clay mineral formation, Geochim. Cosmochim. Acta, 191, 102–117,
775 doi:10.1016/j.gca.2016.07.022, 2016.
776 Frings, P. J., Clymans, W., Fontorbe, G., De La Rocha, C. L. and Conley, D. J.: The continental Si cycle
777 and its impact on the ocean Si isotope budget, Chem. Geol., 425, 12–36,
778 doi:10.1016/j.chemgeo.2016.01.020, 2016.
779 Geilert, S., Vroon, P. Z., Roerdink, D. L., Van Cappellen, P. and van Bergen, M. J.: Silicon isotope
780 fractionation during abiotic silica precipitation at low temperatures: inferences from flow-
781 through experiments, Geochim. Cosmochim. Acta, 142, 95–114,
782 doi:10.1016/j.gca.2014.07.003, 2014.
783 Geilert, S., Vroon, P. Z., Keller, N. S., Gudbrandsson, S., Stefánsson, A. and van Bergen, M. J.: Silicon
784 isotope fractionation during silica precipitation from hot-spring waters: Evidence from the
785 Geysir geothermal field, Iceland, Geochim. Cosmochim. Acta, 164,
786 doi:10.1016/j.gca.2015.05.043, 2015.
787 Geilert, S., Vroon, P. Z. and van Bergen, M. J.: Effect of diagenetic phase transformation on the silicon
788 isotope composition of opaline sinter deposits of Geysir, Iceland, Chem. Geol., 433,
789 doi:10.1016/j.chemgeo.2016.04.008, 2016.
790 Geilert, S., Hensen, C., Schmidt, M., Liebetrau, V., Scholz, F., Doll, M., Deng, L., Fiskal, A., Lever, M. A.,
791 Su, C.-C., Schlömer, S., Sarkar, S., Thiel, V. and Berndt, C.: On the formation of hydrothermal
792 vents and cold seeps in the Guaymas Basin, Gulf of California, Biogeosciences, 15, 5715–5731
793 [online] Available from: https://doi.org/10.5194/bg-15-5715-2018, 2018.
794 Georg, R. B., Reynolds, B. C., Frank, M. and Halliday, A. N.: Mechanisms controlling the silicon
795 isotopic compositions of river waters, Earth Planet. Sci. Lett., 249(3–4), 290–306,
796 doi:10.1016/j.epsl.2006.07.006, 2006a.
797 Georg, R. B., Reynolds, B. C., Frank, M. and Halliday, A. N.: New sample preparation techniques for
798 the determination of Si isotopic compositions using MC-ICPMS, Chem. Geol., 235(1–2), 95–
799 104, doi:10.1016/j.chemgeo.2006.06.006, 2006b.

Georg, R. B., Zhu, C., Reynolds, B. C. and Halliday, A. N.: Stable silicon isotopes of groundwater, feldspars, and clay coatings in the Navajo Sandstone aquifer, Black Mesa, Arizona, USA, Geochim. Cosmochim. Acta, 73(8), 2229–2241, doi:10.1016/j.gca.2009.02.005, 2009.

Gieskes, J. M., Kastner, M., Einsele, G., Kelts, K. and Niemitz, J.: Hydrothermal Activity in the Guaymas Basin, Gulf of California: A synthesis, in In Initial Reports of the Deep Sea Drilling Project. vol. 64, Pt. 2, edited by J. Blakeslee, L. W. Platt, and L. N. Stout, pp. 1159–1167., 1982.

Gieskes, J. M., Simoneit, B. R. T., Brown, T., Shaw, T., Wang, Y. C. and Magenheim, A.: Hydrothermal fluids and petroleum in surface sediments of Guaymas Basin, Gulf of California: A case study, Can. Mineral., 26, 589–602 [online] Available from: http://canmin.geoscienceworld.org/cgi/reprint/26/3/589, 1988.

Gieskes, J. M., Gamo, T. and Brumsack, H.: Chemical methods for interstitial water analysis aboard Joides Resolution, Ocean Drill. Prog. Tech. Note 15. Texas A&M Univ. Coll. Stn., 1991.

Golubev, S. V, Bauer, A. and Pokrovsky, O. S.: Effect of pH and organic ligands on the kinetics of smectite dissolution at 25 ° C, Geochim. Cosmochim. Acta, 70, 4436–4451, doi:10.1016/j.gca.2006.06.1557, 2006.

Grasse, P., Ehlert, C. and Frank, M.: The influence of water mass mixing on the dissolved Si isotope composition in the Eastern Equatorial Pacific, Earth Planet. Sci. Lett., 380, 60–71, doi:10.1016/j.epsl.2013.07.033, 2013.

Grasse, P., Ryabenko, E., Ehlert, C., Altabet, M. A. and Frank, M.: Silicon and nitrogen cycling in the upwelling area off Peru: A dual isotope approach, Limnol. Oceanogr., 61(5), 1661–1676, doi:10.1002/lno.10324, 2016.

Grasse, P., Brzezinski, M. A., Cardinal, D., de Souza, G. F., Andersson, P., Closset, I., Cao, Z., Dai, M., Ehlert, C., Estrade, N., François, R., Frank, M., Jiang, G., Jones, J. L., Kooijman, E., Liu, Q., Lu, D., Pahnke, K., Ponzevera, E., Schmitt, M., Sun, X., Sutton, J. N., Thil, F., Weis, D., Wetzel, F., Zhang, A., Zhang, J. and Zhang, Z.: GEOTRACES inter-calibration of the stable silicon isotope composition of dissolved silicic acid in seawater, J. Anal. At. Spectrom., 32(3), 562–578, doi:10.1039/C6JA00302H, 2017.

Hughes, H. J., Delvigne, C., Korntheuer, M., de Jong, J., André, L. and Cardinal, D.: Controlling the mass bias introduced by anionic and organic matrices in silicon isotopic measurements by MC-ICP-MS, J. Anal. At. Spectrom., 26(9), 1892, doi:10.1039/c1ja10110b, 2011.

Hurd, D. C.: Interactions of biogenic opal , sediment and seawater in the Central Equatorial Pacific, Geochemica Cosmochim. Acta, 37, 2257–2282, 1973.

Kastner, M.: Evidence for Two Distinct Hydrothermal Systems in the Guaymas Basin, in In Initial Reports of the Deep Sea Drilling Project. vol. 64, Pt. 2, edited by J. Blakeslee, L. W. Platt, and L. N. Stout, pp. 1143–1157, U.S. Govt. Printing Office, Washington., 1982.

Kastner, M. and Siever, R.: Siliceous Sediments of the Guaymas Basin: The Effect of High Thermal Gradients on Diagenesis, J. Geol., 91(6), 629–641, doi:10.1086/628816, 1983.

Köhler, S. J., Bosbach, D. B. and Oelkers, E. H.: Do clay mineral dissolution rates reach steady state?, Geochim. Cosmochim. Acta, 69(8), 1997–2006, doi:10.1016/j.gca.2004.10.015, 2005.

De La Rocha, C. L., Brzezinski, M. A. and DeNiro, M. J.: Fractionation of silicon isotopes by marine diatoms during biogenic silica formation, Geochim. Cosmochim. Acta, 61(23), 5051–5056, doi:10.1016/S0016-7037(97)00300-1, 1997.

De La Rocha, C. L., Brzezinski, M. A. and Deniro, M. J.: A first look at the distribution of the stable isotopes of silicon in natural waters, Geochim. Cosmochim. Acta, 64(14), 2467–2477, doi:10.1016/S0016-7037(00)00373-2, 2000.

Lewin, J. C.: The dissolution of silica from diatom walls, Geochim. Cosmochim. Acta, 21(3–4), 182–198, doi:10.1016/S0016-7037(61)80054-9, 1961.

Liu, G., Qiu, S., Liu, B., Pu, Y., Gao, Z., Wang, J., Jin, R. and Zhou, J.: Microbial reduction of Fe(III)-bearing clay minerals in the presence of humic acids, Sci. Rep., 7(9), doi:10.1038/srep45354, 2017.

Lizarralde, D., Soule, S. A., Seewald, J. S. and Proskurowski, G.: Carbon release by off-axis magmatism in a young sedimented spreading centre, Nat. Geosci., 4(1), 50–54, doi:10.1038/ngeo1006, 2010.

Loucaides, S., Michalopoulos, P., Presti, M., Koning, E., Behrends, T. and Van Cappellen, P.: Seawater-mediated interactions between diatomaceous silica and terrigenous sediments: Results from long-term incubation experiments, Chem. Geol., 270(1–4), 68–79, doi:10.1016/j.chemgeo.2009.11.006, 2010.

Lovley, D. R., Fraga, J. L., Blunt-Harris, E. L., Hayes, L. A., Phillips, E. J. P. and Coates, J. D.: Humic Substances as a Mediator for Microbially Catalyzed Metal Reduction, Acta Hydrochim. hydrobiol, 26, 152–157, 1998.

Lupton, J. E.: Helium-3 in the Guaymas Basin: Evidence for injection of mantle volatiles in the Gulf of California, J. Geophys. Res., 84(B13), 7446, doi:10.1029/JB084iB13p07446, 1979.

Mackenzie, F. T., Ristvet, B. L., Thorstenson, D. C., Lerman, A. and Leeper, R. H.: Reverse weathering and chemical mass balance in a coastal environment, in River Inputs to Ocean Systems, edited by J. M. Marten, J. D. Burton, and D. Eisma, pp. 152–187, UNEP and UNESCO, Switzerland., 1981.

McManus, J., Hammond, D. E., Berelson, W. M., Kilgore, T. E., Demaster, D. J., Ragueneau, O. G. and Collier, R. W.: Early diagenesis of biogenic opal: Dissolution rates, kinetics, and paleoceanographic implications, Deep. Res. Part II, 42(2–3), 871–903, doi:10.1016/0967-0645(95)00035-O, 1995.

Méheut, M., Lazzeri, M., Balan, E. and Mauri, F.: Equilibrium isotopic fractionation in the kaolinite, quartz, water system: Prediction from first-principles density-functional theory, Geochim. Cosmochim. Acta, 71(13), 3170–3181, doi:10.1016/j.gca.2007.04.012, 2007.

Michalopoulos, P. and Aller, R. C.: Rapid Clay Mineral Formation in Amazon Delta Sediments: Reverse Weathering and Oceanic Elemental Cycles, Science 270(5236), 614–617, doi:10.1126/science.270.5236.614, 1995.

Michalopoulos, P. and Aller, R. C.: Early diagenesis of biogenic silica in the Amazon delta: Alteration, authigenic clay formation, and storage, Geochim. Cosmochim. Acta, 68(5), 1061–1085, doi:10.1016/j.gca.2003.07.018, 2004.

Michalopoulos, P., Aller, R. C. and Reeder, R. J.: Conversion of diatoms to clays during early diagenesis in tropical, continental shell muds, Geology, 28(12), 1095–1098, doi:10.1130/0091-7613(2000)28<1095:CODTCD>2.0.CO, 2000.

Morley, D. W., Leng, M. J., Mackay, A. W., Sloane, H. J., Rioual, P. and Battarbee, R. W.: Cleaning of lake sediment samples for diatom oxygen isotope analysis, J. Paleolimnol., 31(3), 391–401, doi:10.1023/B:JOPL.0000021854.70714.6b, 2004.

Müller, G.: Methods in sedimentary petrology., in Sedimentary Petrology, Volume 1, edited by W. von Engelhardt, H. Füchtbauer, and G. Müller, pp. 1–283, Schweizerbart, Stuttgart, Germany., 1967.

Müller, P. J. and Schneider, R.: An automated leaching method for the determination of opal in sediments and particulate matter, Deep. Res. Part I, 40(3), 425–444, doi:10.1016/0967-0637(93)90140-X, 1993.

Ng, C. H., Cassarino, L., Pickering, R. A., Woodward, E. M. S., Hammond, S. J. and Hendry, K. R.: Sediment efflux of silicon on the Greenland margin and implications for the marine silicon cycle, Earth Planet. Sci. Lett., 529, 115877, doi:10.1016/j.epsl.2019.115877, 2020.

Oelze, M., von Blanckenburg, F., Bouchez, J., Hoellen, D. and Dietzel, M.: The effect of Al on Si isotope fractionation investigated by silica precipitation experiments, Chem. Geol., 397, 94–105, doi:10.1016/j.chemgeo.2015.01.002, 2015.

Opfergelt, S. and Delmelle, P.: Silicon isotopes and continental weathering processes: Assessing controls on Si transfer to the ocean, Comptes Rendus - Geosci., 344(11–12), 723–738, doi:10.1016/j.crte.2012.09.006, 2012.

Opfergelt, S., Cardinal, D., André, L., Delvigne, C., Bremond, L. and Delvaux, B.: Variations of δ30Si and Ge/Si with weathering and biogenic input in tropical basaltic ash soils under monoculture, Geochim. Cosmochim. Acta, 74(1), 225–240, doi:10.1016/j.gca.2009.09.025, 2010.

Opfergelt, S., Burton, K. W., Pogge von Strandmann, P. A. E., Gislason, S. R. and Halliday, A. N.:

905 Riverine silicon isotope variations in glaciated basaltic terrains: Implications for the Si delivery
906 to the ocean over glacial-interglacial intervals, Earth Planet. Sci. Lett.,(369–370), 211–219,
907 doi:10.1016/j.epsl.2013.03.025, 2013.
908 Parkhurst, B. D. L. and Appelo, C. A. J.: User's Guide To PHREEQC (version 2) — a Computer Program
909 for Speciation, and Inverse Geochemical Calculations, Exch. Organ. Behav. Teach. J.,
910 D(Version 2), 326, doi:Rep. 99-4259, 1999.
911 Petschick, R., Kuhn, G. and Gingele, F.: Clay mineral distribution in surface sediments of the South
912 Atlantic: sources, transport, and relation to oceanography, Mar. Geol., 130(3–4), 203–229,
913 doi:10.1016/0025-3227(95)00148-4, 1996.
914 Rabouille, C., Gaillard, J. F., Tréguer, P. and Vincendeau, M. A.: Biogenic silica recycling in surficial
915 sediments across the Polar Front of the Southern Ocean (Indian Sector), Deep. Res. Part II
916 Top. Stud. Oceanogr., 44(5), 1151–1176, doi:10.1016/S0967-0645(96)00108-7, 1997.
917 Ragueneau, O., Tréguer, P., Leynaert, A., Anderson, R. F., Brzezinski, M. A., DeMaster, D. J., Dugdale,
918 R. C., Dymond, J., Fischer, G., François, R., Heinze, C., Maier-Reimer, E., Martin-Jézéquel, V.,
919 Nelson, D. M. and Quéguiner, B.: A review of the Si cycle in the modern ocean: Recent
920 progress and missing gaps in the application of biogenic opal as a paleoproductivity proxy,
921 Glob. Planet. Change, 26(4), 317–365, doi:10.1016/S0921-8181(00)00052-7, 2000.
922 Rahman, S., Aller, R. C. and Cochran, J. K.: The Missing Silica Sink: Revisiting the Marine Sedimentary
923 Si Cycle Using Cosmogenic 32Si, Global Biogeochem. Cycles, 31(10), 1559–1578,
924 doi:10.1002/2017GB005746, 2017.
925 Reynolds, B. C., Aggarwal, J., André, L., Baxter, D., Beucher, C., Brzezinski, M. A., Cardinal, D.,
926 Engström, E., Georg, R. B., Land, M., Leng, M. J., Opfergelt, S., Rodushkin, I., Sloane, H. J., van
927 den Boorn, S. H. J. M., Vroon, P. Z. and Cardinal, D.: An inter-laboratory comparison of Si
928 isotope reference materials, J. Anal. Atom. Spectrom, 22, 561–568, doi:10.1039/b616755a,
929 2007.
930 Reynolds, B. C., Frank, M. and Halliday, A. N.: Evidence for a major change in silicon cycling in the
931 subarctic North Pacific at 2 . 73 Ma, Paleoceanography, 23(PA4219),
932 doi:10.1029/2007PA001563, 2008.
933 Rickert, D.: Dissolution kinetics of biogenic silica in marine environments, Ber.Polarforschung, 351
934 [online] Available from: ISSN 0176-5027, 2000.
935 Rickert, D., Schlüter, M. and Wallmann, K.: Dissolution kinetics of biogenic silica from the water
936 column to the sediments, Geochim. Cosmochim. Acta, 66(3), 439–455, doi:10.1016/S0016-
937 7037(01)00757-8, 2002.
938 Roerdink, D. L., van den Boorn, S. H. J. M., Geilert, S., Vroon, P. Z. and van Bergen, M. J.: Experimental
939 constraints on kinetic and equilibrium silicon isotope fractionation during the formation of

940 non-biogenic chert deposits, Chem. Geol., 402, 40–51, doi:10.1016/j.chemgeo.2015.02.038,
941 2015.
942 Savage, P. S., Georg, R. B., Armytage, R. M. G., Williams, H. M. and Halliday, A. N.: Silicon isotope
943 homogeneity in the mantle, Earth Planet. Sci. Lett., 295(1–2), 139–146,
944 doi:10.1016/j.epsl.2010.03.035, 2010.
945 Sayles, F. L., Martin, W. R., Chase, Z. and Anderson, R. F.: Benthic remineralization and burial of
946 biogenic SiO2 , CaCO3 , organic carbon , and detrital material in the Southern Ocean along a
947 transect at 170° West, Deep. Res. Part II, 48, 4323–4383, 2001.
948 Scholz, F., Schmidt, M., Hensen, C., Geilert, S., Gutjahr, M. and Liebetrau, V.: Shelf-to-basin iron
949 shuttle in the Guaymas Basin, Gulf of California, Geochim. Cosmochim. Acta, 261, 76–92,
950 doi:10.1016/j.gca.2019.07.006, 2019.
951 Shemesh, A., Mortlock, R. A., Smith, R. J. and Froelich, P. N.: Determination of Ge/Si in Marine
952 Siliceous Microfossils: Separation, Cleaning and Dissolution of Diatoms and Radiolaria, Mar.
953 Chem., 25, 305–323, 1988.
954 de Souza, G. F., Reynolds, B. C., Rickli, J., Frank, M., Saito, M. A., Gerringa, L. J. A. and Bourdon, B.:
955 Southern Ocean control of silicon stable isotope distribution in the deep Atlantic Ocean,
956 Global Biogeochem. Cycles, 26(2), 1–13, doi:10.1029/2011GB004141, 2012.
957 de Souza, G. F., Slater, R. D., Dunne, J. P. and Sarmiento, J. L.: Deconvolving the controls on the deep
958 ocean's silicon stable isotope distribution, Earth Planet. Sci. Lett., 398, 66–76,
959 doi:10.1016/j.epsl.2014.04.040, 2014.
960 de Souza, G. F., Slater, R. D., Hain, M. P., Brzezinski, M. A. and Sarmiento, J. L.: Distal and proximal
961 controls on the silicon stable isotope signature of North Atlantic Deep Water, Earth Planet.
962 Sci. Lett., 432, 342–353, doi:10.1016/j.epsl.2015.10.025, 2015.
963 Sutton, J. N., Varela, D. E., Brzezinski, M. A. and Beucher, C. P.: Species-dependent silicon isotope
964 fractionation by marine diatoms, Geochim. Cosmochim. Acta, 104, 300–309,
965 doi:10.1016/j.gca.2012.10.057, 2013.
966 Sutton, J. N., André, L., Cardinal, D., Conley, D. J., de Souza, G. F., Dean, J., Dodd, J., Ehlert, C.,
967 Ellwood, M. J., Frings, P. J., Grasse, P., Hendry, K., Leng, M. J., Michalopoulos, P., Panizzo, V.
968 N. and Swann, G. E. A.: A Review of the Stable Isotope Bio-geochemistry of the Global Silicon
969 Cycle and Its Associated Trace Elements, Front. Earth Sci., 5(January),
970 doi:10.3389/feart.2017.00112, 2018.
971 Tatzel, M., von Blanckenburg, F., Oelze, M., Schuessler, J. A. and Bohrmann, G.: The silicon isotope
972 record of early silica diagenesis, Earth Planet. Sci. Lett., 428, 293–303,
973 doi:10.1016/j.epsl.2015.07.018, 2015.
974 Teske, A., Callaghan, A. V. and LaRowe, D. E.: Biosphere frontiers of subsurface life in the sedimented

hydrothermal system of Guaymas Basin, Front. Microbiol., 5(JULY), 1–11, doi:10.3389/fmicb.2014.00362, 2014.

Thunell, R. C., Pride, C. J., Tappa, E. and Muller-Karger, F. E.: Biogenic silica fluxes and accumulation rates in the Gulf of California, Geology, 22, 303–306, doi:10.1130/0091-7613(1994)022<0303, 1994.

Tréguer, P. and Pondaven, P.: Silica control of carbon dioxide, Nature, 406, 358–359, doi:10.1080/00207238608710255, 2000.

Tréguer, P. J. and De La Rocha, C. L.: The World Ocean Silica Cycle, Ann. Rev. Mar. Sci., 5(1), 120725114348000, doi:10.1146/annurev-marine-121211-172346, 2013.

Varela, D. E., Pride, C. J. and Brzezinski, M. A.: Biological fractionation of silicon isotopes in Southern Ocean surface waters, Global Biogeochem. Cycles, 18(1), 1–8, doi:10.1029/2003GB002140, 2004.

Viers, J., Dupré, B. and Gaillardet, J.: Chemical composition of suspended sediments in World Rivers : New insights from a new database, Sci. Total Environ., 407(2), 853–868, doi:10.1016/j.scitotenv.2008.09.053, 2009.

Vogt, C., Lauterjung, J. and Fischer, R. X.: INVESTIGATION OF THE CLAY FRACTION (<2µm) OF THE CLAY MINERALS SOCIETY REFERENCE CLAYS, Clays Clay Miner., 50(3), 388–400, 2002.

Wallmann, K., Aloisi, G., Haeckel, M., Tishchenko, P., Pavlova, G., Greinert, J., Kutterolf, S. and Eisenhauer, A.: Silicate weathering in anoxic marine sediments, Geochim. Cosmochim. Acta, 72(12), 2895–2918, doi:10.1016/j.gca.2008.03.026, 2008.

Wetzel, F., de Souza, G. F. and Reynolds, B. C.: What controls silicon isotope fractionation during dissolution of diatom opal?, Geochim. Cosmochim. Acta, 131, 128–137, doi:10.1016/j.gca.2014.01.028, 2014.

Zambardi, T. and Poitrasson, F.: Precise Determination of Silicon Isotopes in Silicate Rock Reference Materials by MC-ICP-MS, Geostand. Geoanalytical Res., 35(1), 89–99, doi:10.1111/j.1751-908X.2010.00067.x, 2011.

Zheng, X., Beard, B. L., Reddy, T. R., Roden, E. E. and Johnson, C. M.: Abiologic silicon isotope fractionation between aqueous Si and Fe(III)-Si gel in simulated Archean seawater : Implications for Si isotope records in Precambrian sedimentary rocks, Geochemica Cosmochim. Acta, 187, 102–122, 2016.

Ziegler, K., Chadwick, O., Brzezinski, M. and Kelly, E. F.: Natural variations of δ30Si ratios during progressive basalt weathering, Hawaiian Islands, Geochim. Cosmochim. Acta, 69(19), 4597–4610, doi:10.1016/j.gca.2005.05.008, 2005a.

Ziegler, K., Chadwick, O., White, A. F. and Brzezinski, M.: δ30Si systematics in a granitic saprolite, Puerto Rico, Geology, 33(10), 817–820, doi:10.1130/G21707.1, 2005b.

Tables

Table 1: Pore fluid Si concentration (µM), $\delta^{30}Si_{pf}$ values (‰) as well as biogenic silica weight fraction ($bSiO_2$ in wt%), Al/Si ratio (mM/M), $\delta^{30}Si_{bSiO2}$ values (‰), porosity (Ø), Al and K contents (wt%) for the basin sites, hydrothermal site, and OMZ site.

Table 2: Water column and hydrothermal plume Si concentration (µM) and Si isotope values (‰). Additionally, the share of hydrothermal fluids within the hydrothermal plume is given based on the calculation provided by Berndt et al. (2016) in their supplementary materials.

Figures

Fig. 1. A) Location map of the sampling stations in the Guaymas Basin, Gulf of California. Black square in the overview map indicates the sampling area. B) Sedimentary $bSiO_2$ content at each sampling station. Water column stations were above MUC15-02 (VCTD02) in the basin, the hydrothermal site (VCTD06, 09), and at the OMZ site (VCTD07).

Fig 2: Depth (cmbsf) profiles for all stations for pore fluid Si concentration ($Si(OH)_4$) in µM (grey symbols) and $\delta^{30}Si_{pf}$ values (colored symbols) and biogenic opal weight fraction ($bSiO_2$) in wt% (grey symbols) and $\delta^{30}Si_{bSiO2}$ values (colored symbols). The dashed line is the $\delta^{30}Si$ value of the deep basin (VCTD02) and the dotted line represents the $\delta^{30}Si$ value of the water column in the OMZ (VCTD07). The uppermost Si isotope data point in the pore fluid diagrams refers to the bottom water (labelled BW). Note the different depth scale for the OMZ site. The brackets around the MUC22-04 bottom water Si concentration value indicate possible surface water contamination. Error bars not indicated are within symbol size. The long-term error (2SD) of international standards is indicated in the upper right $\delta^{30}Si_{pf}$-depth profile.

Fig. 3. Pore fluid $\delta^{30}Si$ values are displayed versus the inverse Si concentration (1/Si) for the basin sites, the hydrothermal site, and the OMZ site. Error bars not indicated are within symbol size. Mixing curves are calculated after Eq. (3) between the respective water column and the average $bSiO_2$ $\delta^{30}Si$ value for all sites (see text for details). The grey shaded area indicates the uncertainty on the equilibrium solubility of $bSiO_2$ assuming 900±150µM following Van Cappellen and Qiu(1997a).

Fig. 4. Asymptotic Si concentration (a) and the pore fluid $\delta^{30}Si_{pf}$ values (b) as a function of the terrigenous/$bSiO_2$ ratio for the basin sites, the hydrothermal site, and the OMZ site in the Guaymas

1045 Basin. An exponential increase in Si concentrations with decreasing terrigenous/$bSiO_2$ ratio is
1046 observed, which is not reflected by corresponding systematic changes in $\delta^{30}Si_{pf}$. The values for the
1047 terrigenous/$bSiO_2$ ratio defining the global trend (grey dots) are from the Southern Ocean, Scotia
1048 Sea, Norwegian Sea, NE Atlantic, Juan de Fuca Ridge, Arabian Sea, and the Peru Basin (Van Cappellen
1049 and Qiu, 1997a; Rabouille et al., 1997; Rickert, 2000).
1050
1051 Fig. 5. Conceptual model of the processes influencing pore fluid $\delta^{30}Si_{pf}$ values in the Guaymas Basin
1052 (a) and the Peruvian margin after Ehlert et al. (2016) (b). Bold values in the sediment show the
1053 average pore fluid $\delta^{30}Si_{pf}$ values. Arrow length indicates the dominating process (dissolution versus
1054 precipitation). The $\delta^{30}Si$ values in the hydrothermal plume indicate dilution with seawater (see
1055 section 4.5). (c) The average pore fluid $\delta^{30}Si_{pf}$ values are shown, indicating the dominance of
1056 precipitation or dissolution processes for the three settings in the Guaymas Basin and the Peruvian
1057 OMZ.
1058
1059 Fig. 6. Data and model results for OMZ core. a: Porosity. b: Biogenic opal concentration in solid
1060 phase. c: K/Al ratio in solid phase. d: Dissolved Si concentration in pore fluids. e: Dissolved potassium
1061 in pore fluids. f: Isotopic composition of dissolved Si. g: rate of biogenic opal dissolution. h: Rate of
1062 authigenic phase precipitation. i: Rate of terrigenous phase dissolution. Sensitivity tests of the model
1063 are indicated by setting the dissolution of terrigenous clay phases to zero (red dashed line) and
1064 setting the precipitation of authigenic phases to zero (black dashed line). The model values agree
1065 best to the measured data when both processes take place (blue line, best fit).

Table 1

Station/MUC#/ Station name	Latitude (N) / Longitude (W)	Water depth	Depth	Pore fluid			Sediment						
				Si	$\delta^{30}Si_{pf}$	2SD	$bSiO_2$	(Al/Si) bSiO2	$\delta^{30}Si_{bSiO2}$	2SD	Φ	Al	K*
		(m)	(cmbsf)	(µM)	(‰)	(‰)	(wt%)	(mM/M)	(‰)	(‰)		mg g^{-1}	mg g^{-1}
SO241-33/11/	27° 33.301'	1855	BW	173	1.9	0.2	-	-	-	-		-	-
Basin site	111° 32.883'		0.5	381	1.3	0.2	22.6	39	0.8	0.1	0.932	44.4	13.7
			1.5	455	-	-	23.1	-	-	-	0.920	45.2	13.9
			2.5	563	1.2	0.1	24.2	-	-	-	0.905	46.3	14.1
			3.5	635	-	-	22.4	-	-	-	0.894	-	-
			4.5	685	-	-	-	-	-	-	0.892	49.1	14.7
			6	686	-	-	25.2	-	-	-	0.875	39.2	12.4
			8	*745*	-	-	-	-	-	-	0.857	-	-
			10	726	-	-	21.9	-	-	-	0.852	-	-
			12.5	737	0.9	0.2	18.5	-	-	-	0.826	53.2	16.0
			15.5	750	-	-	14.4	-	-	-	0.800	61.4	17.9
			18.5	751	-	-	14.8	-	-	-	0.787	-	-
			22	712	1.2	0.2	19.6	26	0.8	0.2	0.801	59.5	17.5
SO241-22/04/	27° 28.165'	1839	BW	54	2.0	0.2	-	-	-	-		-	-
Basin site	111° 28.347'		0.5	349	1.0	0.2	11.6	37	0.9	0.2	0.910	57.8	17.0
			1.5	377	-	-	-	-	-	-	0.907	-	-
			2.5	394	-	-	-	-	-	-	0.890	53.6	16.4
			3.5	421	-	-	-	-	-	-	0.897	-	-
			4.5	474	-	-	-	-	-	-	0.895	-	-
			5.5	558	1.1	0.1	10.9	-	-	-	0.893	58.7	17.3
			7	590	-	-	-	-	-	-	0.895	-	-
			9	637	1.2	0.2	13.1	-	-	-	0.890	58.6	17.2
			11	636	-	-	-	-	-	-	0.891	-	-
			13	597	-	-	-	-	-	-	0.895	-	-
			15.5	545	-	-	-	-	-	-	0.896	-	-
			18.5	440	1.5	0.2	7.6	-	-	-	0.895	57.9	17.3
			22	404			-	-	-	-	0.876	-	-
			26	364	1.3	0.2	9.8	71	0.5	0.2	0.842	66.6	19.4

SO241-23/05/	27° 30.282'	1726	BW	216	1.8	0.3	-	-	-	-		-	-
Basin site	111° 40.770'		0.5	485	1.4	0.2	28.2	23	0.9	0.2	0.934	30.3	9.2
			1.5	610	-	-	-	-	-	-	0.921	-	-
			2.5	713	-	-	-	-	-	-	0.921	-	-
			3.5	753	1.3	0.1	30.1	-	-	-	0.923	31.8	9.8
			4.5	751	-	-	-	-	-	-	0.918	-	-
			5.5	726	-	-	-	-	-	-	0.908	33.1	9.8
			7	713	-	-	-	-	-	-	0.904	-	-
			9	731	1.1	0.2	28.3	-	-	-	0.894	35.3	10.6
			11	690	-	-	-	-	-	-	0.879	-	-
			13	651	-	-	-	-	-	-	0.829	-	-
			15.5	663	-	-	-	-	-	-	0.829	27.6	8.0
			18.5	664	-	-	-	-	-	-	0.825	-	-
			22	640	1.3	0.4	21.4	15	0.4	0.1	0.807	27.7	8.1
SO241-15/02/	27°26.925'	1845	BW	178	1.6	0.2	-	-	-	-			-
Basin site	111°29.926'		0.5	474	1.2	0.3	26.7	19	0.9	0.3	0.958	31.5	10.7
			1.5	569	-	-	24.7	-	-	-	0.943	33.9	10.8
			2.5	590	-	-	27.3	-	-	-	0.935	35.7	11.1
			3.5	610	-	-	27.7	-	-	-	0.918	35.9	11.0
			4.5	605	-	-	-	-	-	-	0.927	30.4	9.2
			5.5	607	1.2	0.2	30.4	-	-	-	0.924	37.2	11.3
			7	635	-	-	-	-	-	-	0.908	37.2	11.4
			9	711	-	-	25.2	-	-	-	0.913	34.5	10.6
			11	746	-	-	30.1	-	-	-	0.918	32.0	9.9
			13	673	-	-	-	-	-	-	0.920	32.2	10.2
			15.5	707	1.2	0.2	47.6	-	-	-	0.927	23.9	7.7
			18.5	727	-	-	-	-	-	-	0.929	21.3	6.6
			22	753	-	-	-	-	-	-	0.919	29.4	9.1
			26	737	-	-	-	-	-	-	0.882	46.4	13.9
			30	781	1.2	0.2	23.6	57	1.0	0.2	0.864	51.8	15.4
SO241-66/16/	27° 24.577'	1842	BW	254	1.5	0.2	-	-	-	-			-
Hydrothermal site	111° 23.265'		0.5	427	2.0	0.2	13.3	52	0.8	0.2	0.911	17.4	4.8
			1.5	554	-	-	-	-	-	-	0.900	18.9	5.2

			2.5	702	-	-		-	-	-	0.855	17.4	4.4
			3.5	752	-	-		-	-	-	0.820	16.7	4.1
			4.5	781	-	-		-	-	-	0.808	16.0	3.8
			5.5	781	2.2	0.1	11.0	-	-	-	0.793	15.4	3.5
			6.5	875	-	-	-	-	-	-	0.775	14.8	3.3
			9	877	-	-		-	-	-	0.770	13.4	2.7
			11	892	-	-	7.0	-	-	-	0.742	9.4	1.3
			13	914	-	-	4.7	-	-	-	0.810	17.8	3.9
			15.5	903	-	-	14.6	-	-	-	0.802	21.9	5.4
			18.5	888	1.8	0.1	8.2	35	0.9	0.1	0.620	2.9	-
SO241-29/09/	27°42.410'	665	BW	31	0.8	0.2	-	-	-	-			-
OMZ site	111°13.656'		0.5	247	-0.5	0.3	15.3	-	-	-	0.970	35.1	12.67
			1.5	425	-	-	-	-	-	-	0.954	46.6	14.0
			2.5	458	-0.3	0.1	16.9	-	-	-	0.945	48.9	14.9
			3.5	492	-	-	-	-	-	-	0.947	47.2	14.7
			4.5	569	-	-	-	-	-	-	0.939	48.6	15.0
			5.5	618	0.3	0.2	15.3	-	-	-	0.935	51.1	15.3
			6.5	655	-	-	-	-	-	-	0.928	50.4	15.4
			7.5	735	-	-	-	-	-	-	0.923	53.4	16.2
			9	*763*	0.0	0.2	13.5	-	-	-	0.926	51.8	15.8
			11	754	-	-	-	-	-	-	0.926	39.5	10.1
			13	753	-	-	-				0.929	48.6	14.2
			15	767	-	-	16.23	26	0.8	0.1	0.909	53.3	15.9
			18.5	772	-	-	-	-	-	-	0.913	53.8	15.9
			20.5	781	-0.2	0.2	18.1	-	-	-	0.911	53.3	15.7
			23.5	763	-	-	-	-	-	-	0.906	56.1	16.8
			26.5	765	-	-	-	-	-	-	0.919	47.8	14.5
			29	763	-	-	-	-	-	-	0.929	41.5	12.6
			30	768	-	-	-	-	-	-	0.925	45.9	13.9
			38	760	0.8	0.2	21.9	-	-	-	0.925	45.8	13.5

Φ = porosity

* porosity corrected

Table 2

Cruise-Station/VCTD#/ bottle#/Station name	Latitude (N) / Longitude (W)	Depth	Si	$\delta^{30}Si$	2SD	hydrothermal fluid share*
		(mbsl)	(µM)	(‰)	(‰)	(%)
Water column						
SO241-12/02/ Basin site	27° 26.133 111° 30.268	1844	163	1.5	0.1	0.1
SO241-42/07/ OMZ site	27° 42.411 111° 13.663	586	78	1.5	0.2	0
Hydrothermal plume						
SO241-67/09/06/ Hydrothermal site	27° 24.750 111° 23.240	1800	253	0.7	0.1	2.1
SO241-67/09/09/ Hydrothermal site	27° 24.750 111° 23.240	1800	206	1.4	0.2	0.2
SO241-67/09/12/ Hydrothermal site	27° 24.750 111° 23.240	1800	690	1.0	0.2	5.7

* calculation in Berndt et al. (2016)

Fig. 1

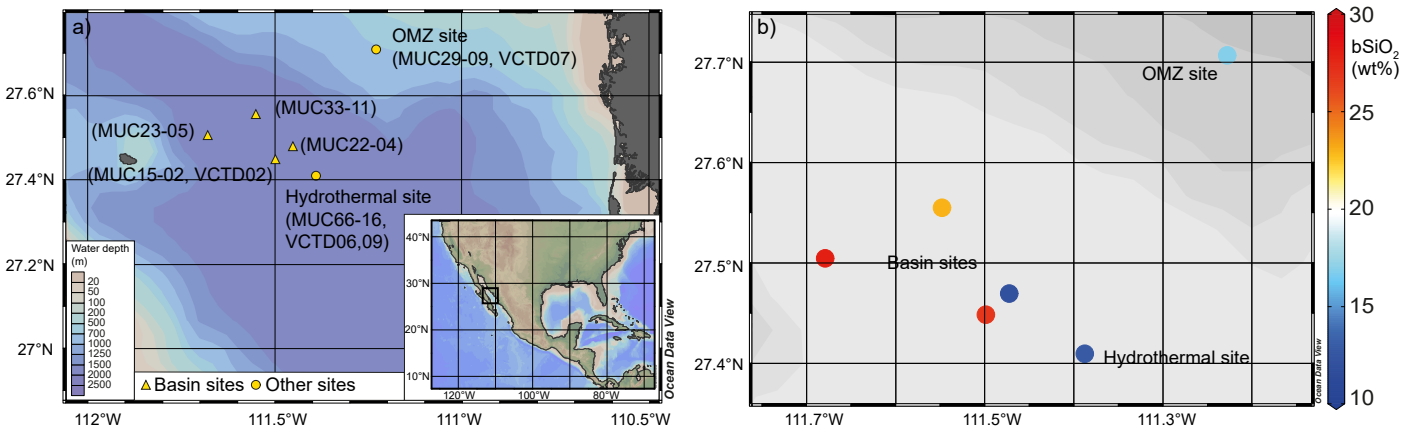
a)
OMZ site
(MUC29-09, VCTD07)
(MUC33-11)
(MUC23-05)
(MUC22-04)
(MUC15-02, VCTD02)
Hydrothermal site
(MUC66-16,
VCTD06,09)
Water depth
(m)
20
50
100
200
500
700
1000
1250
1500
2000
2500
Basin sites
Other sites
27.6°N
27.4°N
27.2°N
27°N
112°W
111.5°W
111°W
110.5°W
40°N
30°N
20°N
10°N
120°W
100°W
80°W
Ocean Data View
b)
OMZ site
Basin sites
Hydrothermal site
27.7°N
27.6°N
27.5°N
27.4°N
111.7°W
111.5°W
111.3°W
30
25
20
15
10
bSiO2
(wt%)
Ocean Data View

Fig. 2

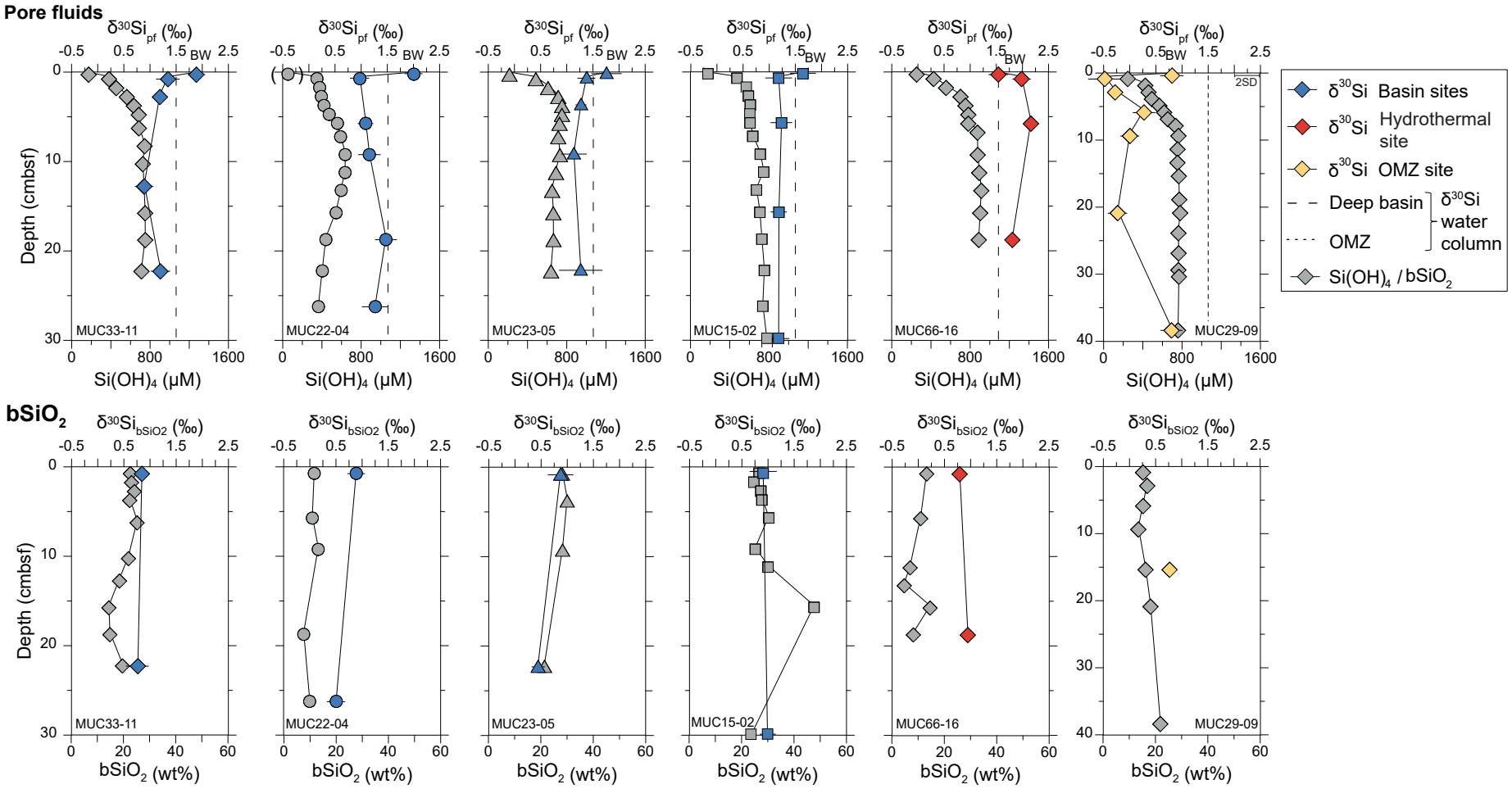
Pore fluids
bSiO2
δ30Si pf (‰)
δ30Si bSiO2 (‰)
BW
2SD
Depth (cmbsf)
Si(OH)4 (μM)
bSiO2 (wt%)
MUC33-11
MUC22-04
MUC23-05
MUC15-02
MUC66-16
MUC29-09
δ30Si Basin sites
δ30Si Hydrothermal site
δ30Si OMZ site
Deep basin
OMZ
δ30Si water column
Si(OH)4 / bSiO2

Fig. 3

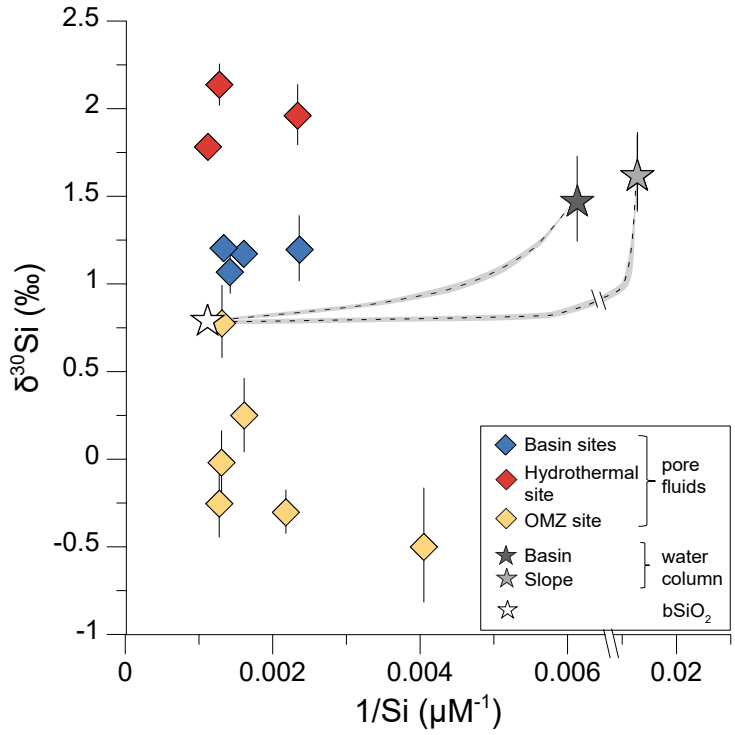
2.5
2
1.5
1
0.5
0
-0.5
-1
δ30Si (‰)
0
0.002
0.004
0.006
0.02
1/Si (μM-1)
Basin sites
Hydrothermal site
OMZ site
pore fluids
Basin
Slope
water column
bSiO2

Fig. 4

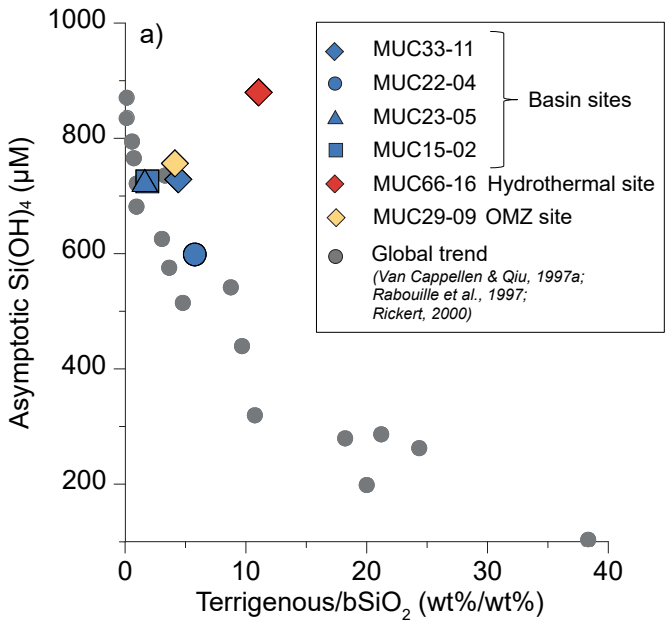
a)
1000
800
600
400
200
0
10
20
30
40
Asymptotic Si(OH)4 (µM)
Terrigenous/bSiO2 (wt%/wt%)
MUC33-11
MUC22-04
MUC23-05
MUC15-02
Basin sites
MUC66-16 Hydrothermal site
MUC29-09 OMZ site
Global trend
(Van Cappellen & Qiu, 1997a;
Rabouille et al., 1997;
Rickert, 2000)

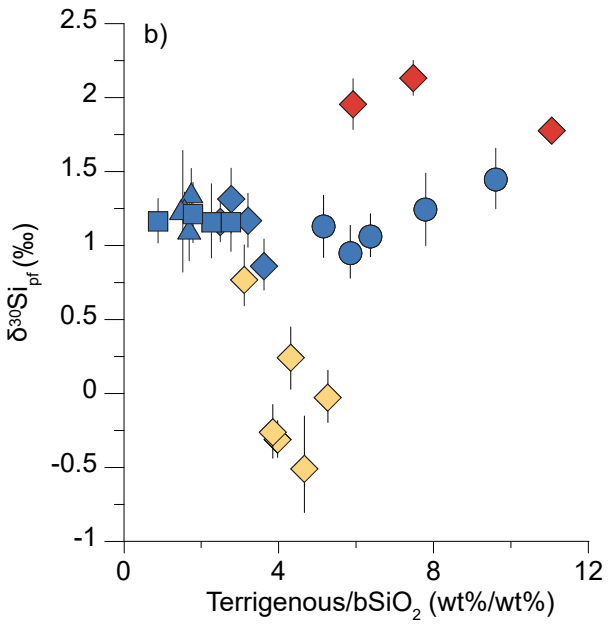
b)
2.5
2
1.5
1
0.5
0
-0.5
-1
0
4
8
12
δ30Sipf (‰)
Terrigenous/bSiO2 (wt%/wt%)

Fig. 5

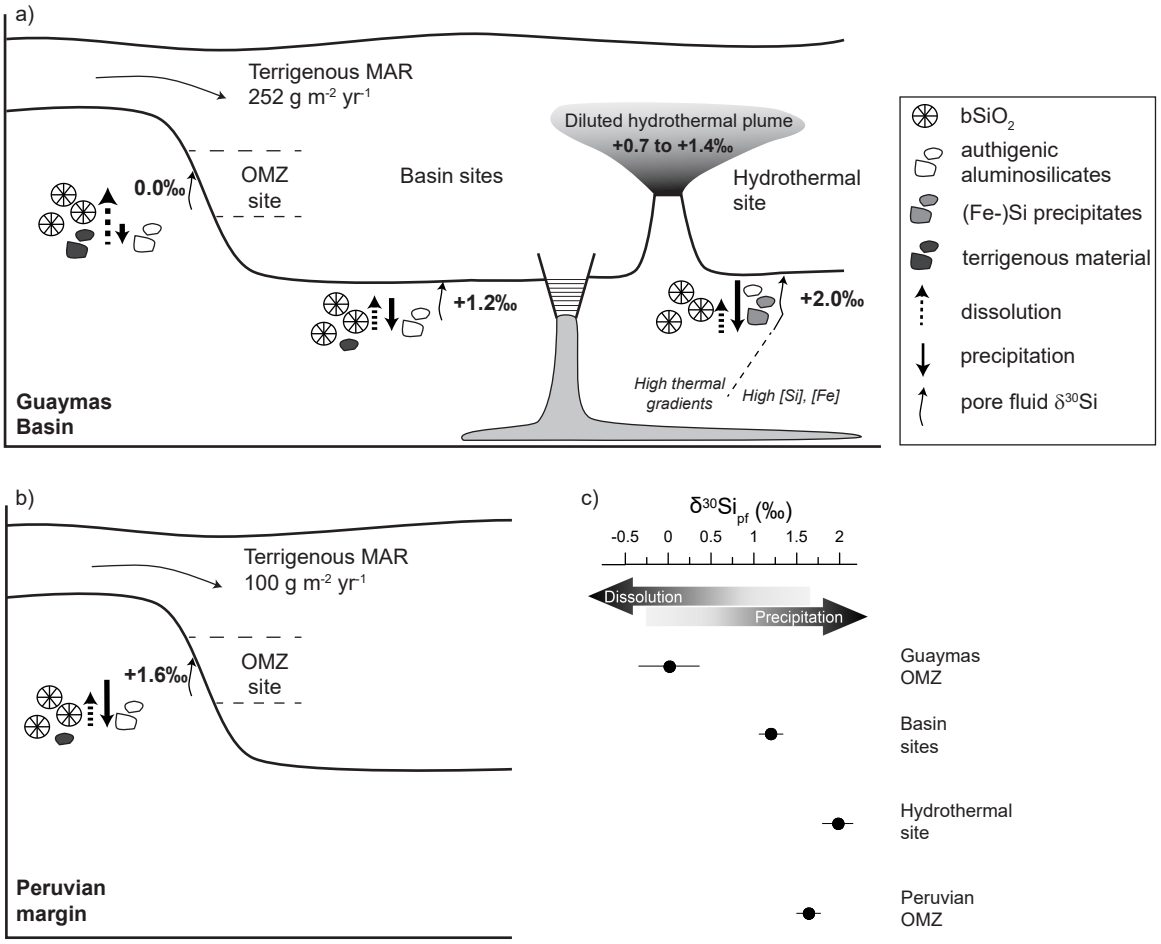
a)
Terrigenous MAR
252 g m-2 yr-1
Diluted hydrothermal plume
+0.7 to +1.4‰
OMZ
site
Basin sites
Hydrothermal
site
0.0‰
+1.2‰
+2.0‰
High thermal
gradients
High [Si], [Fe]
Guaymas
Basin
bSiO2
authigenic
aluminosilicates
(Fe-)Si precipitates
terrigenous material
dissolution
precipitation
pore fluid δ30Si
b)
Terrigenous MAR
100 g m-2 yr-1
OMZ
site
+1.6‰
Peruvian
margin
c)
δ30Sipf (‰)
-0.5
0
0.5
1
1.5
2
Dissolution
Precipitation
Guaymas
OMZ
Basin
sites
Hydrothermal
site
Peruvian
OMZ

Fig. 6

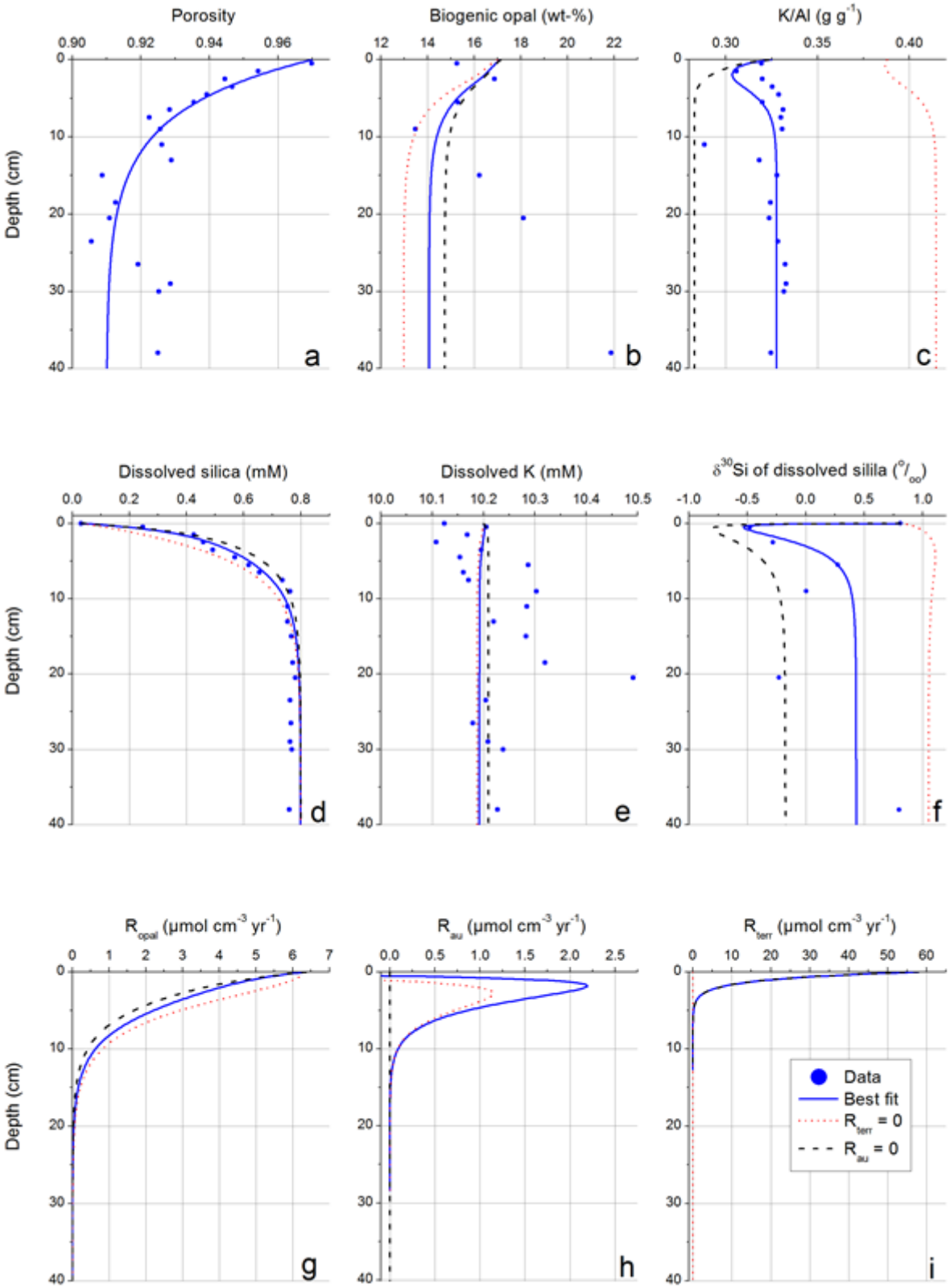
Porosity
Biogenic opal (wt-%)
K/Al (g g-1)
Depth (cm)
a
b
c
Dissolved silica (mM)
Dissolved K (mM)
δ30Si of dissolved silila (‰)
d
e
f
Ropal (μmol cm-3 yr-1)
Rau (μmol cm-3 yr-1)
Rterr (μmol cm-3 yr-1)
g
h
i
Data
Best fit
Rterr = 0
Rau = 0